High-Spin Molecules: Unusual Magnetic Susceptibility Relaxation Effects in $[Mn_{12}O_{12}(O_2CEt)_{16}(H_2O)_3]$ ($S = 9$) and the One-Electron Reduction Product $(PPh_4)[Mn_{12}O_{12}(O_2CEt)_{16}(H_2O)_4]$ ($S = {}^{19}/_2$)

Hilary J. Eppley,[†] Hui-Lien Tsai,[‡] Nadine de Vries,[†,§] Kirsten Folting,[†] George Christou,*[,†] and David N. Hendrickson*[,‡]

Contribution from the Department of Chemistry and Molecular Structure Center, Indiana University, Bloomington, Indiana 47405-4001, and the Department of Chemistry-0358, University of California at San Diego, La Jolla, California 92093-0358

Received August 8, 1994[⊗]

Abstract: Treatment of $[Mn_{12}O_{12}(O_2CMe)_{16}(H_2O)_4]$ (**1**) with an excess of $EtCO_2H$ in toluene leads to high yield (~70%) conversion to $[Mn_{12}O_{12}(O_2CEt)_{16}(H_2O)_3]$ (**3**). Complex **3**·$4H_2O$ crystallizes in the triclinic space group $P\bar{1}$, which at −165 °C has $a = 13.851(3)$ Å, $b = 23.431(5)$ Å, $c = 13.663(3)$ Å, $\alpha = 103.76(1)°$, $\beta = 111.46(1)°$, $\gamma = 78.13(1)°$, and $Z = 2$. The structure was refined with 8470 observed [$F > 3.0\sigma(F)$] reflections to give $R = 6.07$ and $R_w = 6.21\%$. The complex consists of a central $[Mn^{IV}_4O_4]^{8+}$ cubane held within a nonplanar ring of eight Mn^{III} atoms by eight μ_3-O^{2-} ions. One of the Mn^{III} ions is five coordinate. NMR (^1H,^{19}F) studies on $[Mn_{12}O_{12}(O_2CR)_{16}(H_2O)_4]$ (R = Me, Et, and substituted Ph) show that the dodecanuclear species retain their structural integrity upon dissolution in CD_3CN. The spectra show four carboxylate resonances, consistent with effective D_2 minimal symmetry in solution. Electrochemical studies on **1**−**3** and a series of related species show a quasireversible reduction in the 0.00 to 0.47 V range, and a quasireversible oxidation in the 0.70 to 1.07 V range, together with additional mostly irreversible oxidation and reduction processes. Reduction of complex **3** with PPh_4I in CH_2Cl_2 leads to isolation of $(PPh_4)[Mn_{12}O_{12}(O_2CEt)_{16}(H_2O)_4]$ (**4**) in ~70% yield. Complex **4** crystallizes in monoclinic space group $P2_1/c$ with the following cell dimensions at −168 °C: $a = 13.046(4)$, $b = 28.223(9)$, $c = 27.162(8)$ Å, $\beta = 96.32(1)°$, $Z = 4$, and $V = 9940.45$ Å^3. The structure was refined using 9871 unique reflections with $I > 3\sigma(I)$ to give $R = 6.51$ and $R_w = 6.65\%$, respectively. The structure shows that the added electron is localized on an outer (originally Mn^{III}) ion rather than an inner (cubane) Mn^{IV} ion, producing a trapped-valence $Mn^{II}Mn^{III}_7Mn^{IV}_4$ anion. The results of dc and ac magnetic susceptibility studies are described. DC studies of complexes **3**·H_2O (**3a**) and **4** in a 10 kG field show maxima in the μ_{eff}/Mn_{12} *vs* *T* plots at ~18.5−19.0 μ_B in the ~15−20 K range, consistent with ground states with relatively large spins. In order to determine the magnitude of the latter, additional dc (2.0−4.0 K, 20−50 kG fields) and ac (2.0−30 K, 1.0 and 0.0050 G fields, 25−1000 Hz frequencies) data were collected. Analysis of these data show that complex **3a** has an $S = 9$ ground state, and that complex **4** has an $S = {}^{19}/_2$ ground state. Furthermore, χ'_MT values for complex **4**, where χ'_M is the in-phase component of the ac susceptibility, exhibit a plateau in the 6−16 K range, below which there is an abrupt decrease in χ'_MT. Related to this is the observation that χ''_M, the out-of-phase component of the ac susceptibility, has a nonzero value that is frequency dependent. This is extremely rare and unusual behavior, seen previously in discrete species only for complex **1** and its $PhCO_2^-$ analogue complex **2**. Frequency-dependent χ''_M values are normally seen for superparamagnetic materials. Complex **3a** exhibits two peaks in the χ''_M *vs* *T* plot; hence, two different relaxation processes are seen. When an ac field oscillating at 500 Hz is used, for example, the two χ''_M peaks occur at 2.8 and 6.4 K. Upon reexamination of the ac susceptibilities of complexes **1** and **2**, it was found that they also show a second low-temperature χ''_M peak. Polystyrene-doped (3.6 and 54 wt %) samples of complex **3a** also show two χ''_M peaks. DC susceptibility data for complexes **3a**, **4**, and polystyrene-doped **3a** show that these complexes exhibit well-developed hysteresis loops. Furthermore, zero-field-cooled and field-cooled magnetization data for complexes **3a** and **4** are not superimposed at the lowest temperatures. All of these data reflect the presence of relaxation processes. The fact that the same observations are made for the polystyrene-doped sample of complex **3a** indicates that the hysteresis/relaxation processes are attributable to properties of individual molecules, rather than from a bulk effect of the material.

Introduction

Nanoscale magnetic materials are the focus of considerable research because they are expected to exhibit unusual properties.[1] Such nanoscale magnetic materials can be prepared either by fragmenting bulk ferromagnets or by building up molecules to be large enough to show interesting magnetic properties. Recently, Taft *et al.*[2] and Papaefthymiou[3] employed Mössbauer spectroscopy to demonstrate the presence of superparamagnetism in Fe_{12} and Fe_{19} molecular complexes. Only two complexes, $[Mn_{12}O_{12}(O_2CR)_{16}(H_2O)_4]$ [R = CH_3 (**1**) or Ph (**2**)], have been reported[4,5] to exhibit the out-of-phase ac susceptibility

[†] Indiana University.
[‡] University of California at San Diego.
[§] Present address: DuPont Central Research and Development, Wilmington, DE.
[⊗] Abstract published in *Advance ACS Abstracts*, December 1, 1994.

(1) (a) Stamp, P. C. E.; Chudnosvsky, E. M.; Barbara, B. *Int. J. Mod. Phys.* **1992**, *B6*, 1355. (b) McMichael, R. D.; Shull, R. D.; Swartzendruber, L. J.; Bennett, L. H.; Watson, R. E. *J. Magn. Magn. Mater.* **1992**, *111*, 29. (c) Awschalom, D. D.; Di Vincenzo, D. P.; Smyth, J. F. *Science* **1992**, *258*, 414.

0002-7863/95/1517-0301$09.00/0

behavior characteristic of superparamagnetic materials. This out-of-phase ac susceptibility signal for complex **1** has been shown[6] to arise from individual Mn_{12} molecules which exhibit large magnetic anisotropy. This anisotropy is attributable to single-ion zero-field effects influencing an $S = 10$ ground state. Unlike a simple paramagnet, the magnetization in the Mn_{12} complexes **1** and **2** cannot stay in phase with the magnetic field oscillating at a particular frequency in the ac susceptibility experiment. In fact, a single crystal of complex **1** has been reported[6] to show a well developed hysteresis loop in the 2.2–2.8 K range. Zero-field splitting in the high spin ($S = 10$) ground state of complex **1** appears to be the origin of this hysteresis.

Molecules that possess a ground state with a large number of unpaired electrons are also desirable as potential building blocks for molecular-based magnetic materials.[7] High-spin organic molecules with both conjugated π construction[8] and with more localized[9] bonding have been prepared. A hydrocarbon consisting of five carbene linkages and possessing an $S = 6$ ground state has been reported[10] to have the highest spin value for an organic molecule. In the case of inorganic molecules, an $[Mn^{II}_6(nitroxide)_6]$ complex[11] with an $S = 12$ ground state held the record for the highest ground state for several years. Very recently, however, Goldberg *et al.*[12] reported the preparation and characterization of $(Me_4N)_4[Mn_{10}(biphen)_4O_4Cl_{12}]$, where biphen is 2,2′-biphenoxide. This $Mn^{II}_6Mn^{III}_4$ complex was shown to have an $S = 14$ ground state.

In this paper the preparation and characterization of $[Mn_{12}O_{12}(O_2CEt)_{16}(H_2O)_3]$ (**3**), a salt of its singly reduced form, $(PPh_4)[Mn_{12}O_{12}(O_2CEt)_{16}(H_2O)_4]$ (**4**), and some analogous complexes are reported. Not only does complex **4** have an unusual trapped-valence $Mn^{II}Mn^{III}_7Mn^{IV}_4$ structure, but complexes **3** and **4** exhibit interesting magnetic properties as well.

Experimental Section

Compound Preparation. All chemicals and solvents were used as received; all preparations and manipulations were performed under aerobic conditions. $[Mn_{12}O_{12}(O_2CMe)_{16}(H_2O)_4]\cdot 2CH_3CO_2H\cdot 4H_2O$ (**1**)[13] and $[Mn_{12}O_{12}(O_2CPh)_{16}(H_2O)_4]\cdot HO_2CPh\cdot CH_2Cl_2$ (**2**)[4] were prepared as described elsewhere except that the reaction solution for **1** was not heated to 60 °C. The $CD_3CO_2^-$ version of **1** was prepared in an analogous manner using CD_3CO_2D.

$[Mn_{12}O_{12}(O_2CEt)_{16}(H_2O)_3]$ (3). A slurry of complex **1** (3.0 g, 1.5 mmol) in toluene (75 mL) was treated with propionic acid (3.0 mL, 40 mmol). The mixture was concentrated to remove acetic acid as the toluene azeotrope (toluene/CH_3CO_2H = 72/28%). As the solvent volume was reduced, the black solid slowly dissolved. When almost all the toluene had been removed, more toluene (75 mL) was added and removed by evaporation, and the process repeated. The resulting oil was dissolved in toluene (75 mL), filtered, and treated with a further amount of propionic acid (3.0 mL), and the entire process repeated. After the final filtration, hexanes (3 vol equiv) were added and the solution stored at room temperature for 48 h. The resultant, black, star-shaped clusters of crystals were collected by filtration, washed copiously with hexanes and dried *in vacuo*. The overall yield of $3\cdot H_2O$ (**3a**) was ~55%. Selected IR bands (KBr, cm^{-1}): 3370 (m, br), 1586 (s), 1575 (s), 1466 (s), 1432 (vs), 1379 (s), 812 (m), 719 (m), 650 (s, br), 559 (m, br). Conductivity (25 °C): 4.1 and 0.3 S cm^2 mol^{-1} in CH_3CN and CH_2Cl_2, respectively. Anal. Calcd (Found) for $C_{48}H_{88}O_{48}Mn_{12}$: C, 27.55 (27.63); H, 4.24 (4.27); Mn, 31.51 (30.52). Crystals suitable for crystallographic studies were grown by layering a toluene solution of **3** with hexanes. Suitable single crystals of what was subsequently identified as $[Mn_{12}O_{12}(O_2CEt)_{16}(H_2O)_3]\cdot 4H_2O$ ($3\cdot 4H_2O$) were obtained by this procedure; they were kept in contact with mother liquor to prevent solvent loss. The elemental analysis indicates a loss of lattice water upon drying relative to the crystallographically characterized species. A series of complexes analogous to **2**, but with one or more substituents on the phenyl ring, were prepared using methods similar to that for complex **3**, employing the appropriate substituted benzoic acid.

$(PPh_4)[Mn_{12}O_{12}(O_2CEt)_{16}(H_2O)_4]$ (4). To a stirred dark brown solution of complex $3\cdot H_2O$ (2.0 g, 9.5 mmol) in CH_2Cl_2 (30 mL) was added solid PPh_4I (0.45 g, 9.5 mmol). The solution was stirred for an additional 30 min with no noticeable color change. Hexanes (150 mL) were than added, and the flask was left undisturbed overnight at ambient temperature. The resultant thin golden-brown, platelike crystals were collected by filtration, washed with hexanes, toluene (to remove unconverted complex **3**) and Et_2O, and dried *in vacuo*. The yield was typically ~70%. Large needles suitable for X-ray crystallography were grown from CH_2Cl_2/hexanes. Selected IR data (KBr, cm^{-1}): 3400 (w, br), 1568 (vs, br), 1466 (s), 1435 (vs), 1300 (s), 723 (s), 689 (s), 648 (s), 613 (s, b), 527 (s). Conductivity (25 °C): 105 and 50 S cm^2 mol^{-1} in MeCN and CH_2Cl_2, respectively. Anal. Calcd (Found) for $C_{72}H_{108}O_{48}PMn_{12}$: C, 35.56 (35.43); H, 4.48 (4.44); Mn, 27.11 (26.75).

$(NPr^n_4)[Mn_{12}O_{12}(O_2CPh)_{16}(H_2O)_4]\cdot H_2O$ (5). To a stirred dark brown solution of complex **2** (1.0 g, 0.35 mmol) in CH_2Cl_2 (60 mL) was added solid NPr^n_4I (0.11 g, 0.35 mmol). No noticeable color change occurred as the latter dissolved. After 10 min, EtOAc/Et_2O (2:1, 100 mL) was added to give a brown precipitate which was collected by filtration, washed well with EtOAc and Et_2O, and dried *in vacuo*. The yield was typically ~74%. Selected IR data (KBr, cm^{-1}): 3065 (w), 1597 (m), 1557 (m), 1418 (s), 720 (s), 677 (m), 654 (m), 615 (m). Conductivity (MeCN, 25 °C): 97 S cm^2 mol^{-1}. Anal. Calcd (Found) for $C_{124}H_{118}NO_{49}Mn_{12}$: C, 48.58 (48.40); H, 3.88 (3.87); N, 0.46 (0.61); Mn, 21.51 (21.14).

$(PPh_4)[Mn_{12}O_{12}(O_2CPh)_{16}(H_2O)_4]\cdot 2H_2O$ (6). This complex was prepared in a manner analogous to that for **5**, replacing NPr^n_4I with PPh_4I (0.16 g, 0.35 mmol). The yield was typically 82%. Conductivity (MeCN, 25 °C): 107 S cm^2 mol^{-1}. Anal. Calcd (Found) for $C_{136}H_{112}O_{50}PMn_{12}$: C, 50.47 (50.57); H, 3.49 (3.68); Mn, 20.37 (20.60).

$(PPN)[Mn_{12}O_{12}(O_2CPh)_{16}(H_2O)_4]\cdot H_2O$ (7). Complex **2** (0.500 g, 0.175 mmol) and PPNCl (0.100 g, 0.175 mmol) [$PPN^+ = (Ph_3P)_2N^+$] were dissolved in CH_2Cl_2 (25 mL). A solution of KI (0.004 g, 0.265 mmol) in H_2O (12 mL) was added, and the two immiscible phases were stirred together for 45 min. Small amounts of brown amorphous solid were removed by filtration. To the separated organic phase was added an equal volume of hexanes and the solution stored at room temperature for 24 h. The resulting light brown platelike crystals were collected by filtration, washed with hexanes and redissolved in CH_2Cl_2; layering with hexanes slowly produced black needles which were collected by filtration, washed with hexanes and Et_2O, and dried *in vacuo*. The overall yield was ~55%. Conductivity (CH_2Cl_2, 25 °C): 40.4 S cm^2 mol^{-1}. Anal. Calcd (Found) for $C_{148}H_{120}NO_{49}P_2Mn_{12}$: C, 52.01 (51.81); H, 3.54 (3.42); N, 0.41 (0.46); Mn, 19.21 (19.45).

X-ray Crystallography. Data were collected for complexes $3\cdot 4H_2O$ and **4** with a Picker four-circle diffractometer; details of the diffractometry, low-temperature facilities, and computational procedures employed by the Molecular Structure Center are available elsewhere.[14] Suitable single crystals were selected, affixed to glass fibers with silicone grease, and transferred to the goniostat where they were cooled

(2) Taft, K. L.; Papaefthymiou, G. C.; Lippard, S. J. *Science* **1993**, *259*, 1302.
(3) Papaefthymiou, G. C. *Phys. Rev.* **1992**, *B46*, 10366.
(4) Sessoli, R.; Tsai, H.-L.; Schake, A. R.; Wang, S.; Vincent, J. B.; Folting, K.; Gatteschi, D.; Christou, G.; Hendrickson, D. N. *J. Am. Chem. Soc.* **1993**, *115*, 1804.
(5) Caneschi, A.; Gatteschi, D.; Sessoli, R.; Barra, A. L.; Brunel, L. C.; Guillot, M. *J. Am. Chem. Soc.* **1991**, *113*, 5873.
(6) Caneschi, A.; Gatteschi, D.; Sessoli, R.; Novak, M. A. *Nature* **1993**, *365*, 141.
(7) Delfs, C. D.; Gatteschi, D.; Pardi, L. *Comments Inorg. Chem.* **1993**, *15*, 27.
(8) (a) Iwamura, H. *Pure Appl. Chem.* **1987**, *59*, 1595. (b) Iwamura, H. *Pure Appl. Chem.* **1986**, *58*, 187. (c) Itoh, K.; Takui, T.; Teki, Y.; Kinoshita, J. *J. Mol. Elect.* **1988**, *4*, 181.
(9) Dougherty, D. A. *Pure Appl. Chem.* **1990**, *62*, 519.
(10) Nakamura, N.; Inoue, K.; Iwamura, H.; Fujioka, T.; Sawaki, Y. *J. Am. Chem. Soc.* **1992**, *114*, 1484.
(11) Caneschi, A.; Gatteschi, D.; Laugier, J.; Rey, P.; Sessoli, R.; Zanchini, C. *J. Am. Chem. Soc.* **1988**, *110*, 2795.
(12) Goldberg, D. P.; Caneschi, A.; Lippard, S. J. *J. Am. Chem. Soc.* **1993**, *115*, 9299.
(13) Lis, T. *Acta Crystallogr. Sect. B* **1980**, *36*, 2042.

Table 1. Crystallographic Data for Complexes **3**·4H_2O and **4**

	3·4H_2O	**4**
formula[a]	$C_{48}H_{94}O_{51}Mn_{12}$	$C_{72}H_{108}O_{48}PMn_{12}$
formula wt, g/mol	2146.50	2431.85
space group	$P\bar{1}$	$P2_1/c$
a, Å	13.851(3)	13.046(4)
b, Å	23.431(5)	28.223(9)
c, Å	13.663(3)	27.162(8)
α, deg	103.76(1)	90
β, deg	111.46(1)	96.32(1)
γ, deg	78.13(1)	90
V, Å^3	3973.8	9940.5
Z	2	4
T, °C	−165	−168
radiation[b]	0.71069 Å	0.71069 Å
ϱ_{calc}, g/cm^3	1.79	1.63
μ, cm^{-1}	18.624	15.123
octants	+h, ±k, ±l	+h, +k, ±l
total data	12190	15304
unique data	10368	13090
R_{merge}	0.011	0.104
obsd data ($F > 3\sigma(F)$)	8470	9871
$R(R_w)$[c,d]	0.0607 (0.0621)	0.0651 (0.0665)

[a] Formula for **3**·4H_2O includes four H_2O solvate molecules; for **4**, solvate molecules are excluded. [b] Graphite monochromator. [c] $R = \Sigma||F_o| - |F_c||/\Sigma|F_o|$. [d] $R_w = [\Sigma w(|F_o| - |F_c|)^2/\Sigma w|F_o|^2]^{1/2}$ where $w = 1/\sigma^2(|F_o|)$.

for characterization and data collection. Crystallographic data are collected in Table 1. For both complexes, the structures were solved by a combination of direct methods (MULTAN78) and Fourier techniques and refined by full-matrix least squares.

For complex **3**·4H_2O, a systematic search of a limited hemisphere of reciprocal space yielded a set of reflections which exhibited no Laue symmetry (other than $\bar{1}$) and no systematic extinctions. The choice of the triclinic space group $P\bar{1}$ was confirmed by the subsequent solution and refinement of the structure. The intensities of four standard reflections measured every 400 reflections showed no significant decay. No absorption correction was carried out. The 12 Mn atoms were located in the best E-map and the remaining non-hydrogen atoms were located in successive iterations of least-squares refinement and difference Fourier syntheses. The asymmetric unit was found to contain the Mn_{12} complex as well as five peaks [O(113) through O(117)] that could be interpreted as H_2O molecules in the lattice; two of them were located close to centers of symmetry and were assigned 50% occupancy. The lattice also contained a disordered molecule of toluene solvent [C(118) through C(121)] that refined to about 50% occupancy. Two areas of disorder between H_2O and propionate groups were located; one of these involves O(106), O(51), and O(53), with the propionate C atoms having 50% occupancy between O(106) and O(51), and 50% occupancy between O(51) and O(53). Similar observations were made for O(66), O(68), and O(109). A disorder was also observed in the position of propionate C atom C(80). All non-hydrogen atoms were refined with anisotropic thermal parameters; no H atoms were included in the final refinement cycles, except for the two H atoms on water molecule O(25) that were clearly visible in a difference Fourier map. These were included in the final cycles with fixed parameters. The total number of variables refined was 1091. The final difference Fourier map was essentially featureless with the largest peak being 1.3 e/Å^3 near a propionate ethyl group. Final values of $R(R_w)$ are included in Table 1.

For complex **4**, a systematic search of a limited hemisphere of reciprocal space yielded a set of reflections which exhibited monoclinic ($2/m$) symmetry. The systematic extinction of $0k0$ for $k = 2n + 1$ and of $h01$ for $1 = 2n + 1$ uniquely identified the space group as $P2_1/c$ (no. 14). This choice was confirmed by the subsequent solution and refinement of the structure. The intensities of four standard reflections measured every 300 reflections showed no significant decay. No absorption correction was performed. The 12 Mn atoms were located in the best E-map and the remaining non-hydrogen atoms were located in successive iterations of difference Fourier map syntheses. In addition to the Mn_{12} anion and the PPh_4^+ cation, the asymmetric unit was found to contain several (eight) peaks of an unidentified solvent and two atoms that were tentatively identified as water molecules [O(138) and O(139)], because they were within hydrogen bonding distances of oxygen atoms. All of the "solvent" atoms were refined using oxygen scattering factors; an occupancy factor was also refined resulting in occupanices of 100%, 100%, 100%, 70%, 45%, 45%, and 35%, respectively, for atoms O(136) to O(143). As for **3**·4H_2O, a disorder between H_2O and propionate groups was located in the area of O(25), O(74), and O(76). After refining the partially occupied carbon atoms located between these oxygens using isotropic parameters, the occupancy was found to be 65% for C(75) and C(77), and 35% for C(109) and C(110), and thus O(25) was represented in Figure 3 as a bound water. No hydrogen atoms were located and, owing to program limitations, none were included in the refinement. The refinement was completed using anisotropic thermal parameters on all but the disordered atoms. The total number of variables refined was 1257. The final difference map was essentially featureless with three peaks of about 1 e/Å^3 all in the vicinity of propionate ethyl groups. Final values of $R(R_w)$ are included in Table 1.

Physical Measurements. Direct current (dc) magnetic susceptibility measurements were carried out on a Quantum Design MPMS5 SQUID susceptometer equipped with a 55 kG magnet and operating in the range of 1.8−400 K. Alternating current (ac) magnetic susceptibility measurements were carried out on a Quantum Design MPMS2 SQUID ac susceptometer. The ac frequency range is 5.0×10^{-4} to 1.5 kHz and the ac field strength can be varied from 10^{-4} to 2.0 G. Pascal's constants[15] were used to estimate the diamagnetic corrections for each complex, which were subtracted from the experimental susceptibilities to give the molar paramagnetic susceptibilities. The computer program GENSPIN[16] was used to analyze variable-field magnetization data. The spin of the ground state is set at some value, and then the spin Hamiltonian matrix is diagonalized at each magnetic field to least-squares fit the experimental data.

Electrochemical studies were performed under argon, using a BAS Model CV-50W voltammetric analyzer and a standard three-electrode assembly (glassy carbon working, Pt wire auxiliary, SCE reference) with 0.1 M $NBu^n_4PF_6$ as supporting electrolyte. No IR compensation was employed. Quoted potential values are *vs* the ferrocene/ferrocenium couple measured under the same conditions. The scan rate for cyclic voltammetry and differential pulse voltammetry was set at 100 and 20 mV, respectively. Distilled MeCN and CH_2Cl_2 were utilized as solvents. The concentration of the complexes was approximately 1 mM. ^{1}H NMR spectra were recorded at 300 MHz employing a Varian XL-300 spectrometer, using protio-solvent peaks as internal references. ^{19}F NMR spectra were recorded at 339.7 MHz on a Nicolet NT360 spectrometer with $CFCl_3$ and CF_3CO_2H as external references. Conductivity measurements were performed at room temperature on ~0.25 mM solutions employing a YSI 31A conductance bridge and a YSI 3403 dip cell. Infrared spectra were recorded as KBr pellets using a Nicolet 510P FT spectrophotometer. EPR spectra were recorded on toluene/CH_2Cl_2 glasses or crushed solid using a Bruker ESP300 EPR operating at X-band frequencies (9.4 GHz) with a Hewlett-Packard 5350B microwave frequency counter and an Oxford liquid He cryostat and temperature controller. Elemental analyses (C, H, N, P) were performed by Atlantic Microlab, Norcross, GA. Manganese titrations were performed locally.

Results and Discussion

Electrochemistry. In our previous report,[17] we described the electrochemical properties of **1** and **2**, and showed that they exhibit several very similar redox processes. A quantitative comparison of the measured potentials could not be made, however, since the complexes are not soluble in an appropriate

(14) Chisholm, M. F.; Folting, K.; Huffman, J. C.; Kirkpatrick, C. C. *Inorg. Chem.* **1984**, *23*, 1021.

(15) *Theory and Applications of Molecular Paramagnetism*; Boudreaux, E. A., Mulay, L. N., Eds.; J. Wiley & Sons: New York, 1976.

(16) Schunitt, E. A.; Hendrickson, D. N. Unpublished results.

(17) Schake, A. R.; Tsai, H.-L.; de Vries, N.; Webb, R. J.; Folting, K.; Hendrickson, D. N.; Christou, G. *J. Chem. Soc., Chem. Commun.* **1992**, 181.

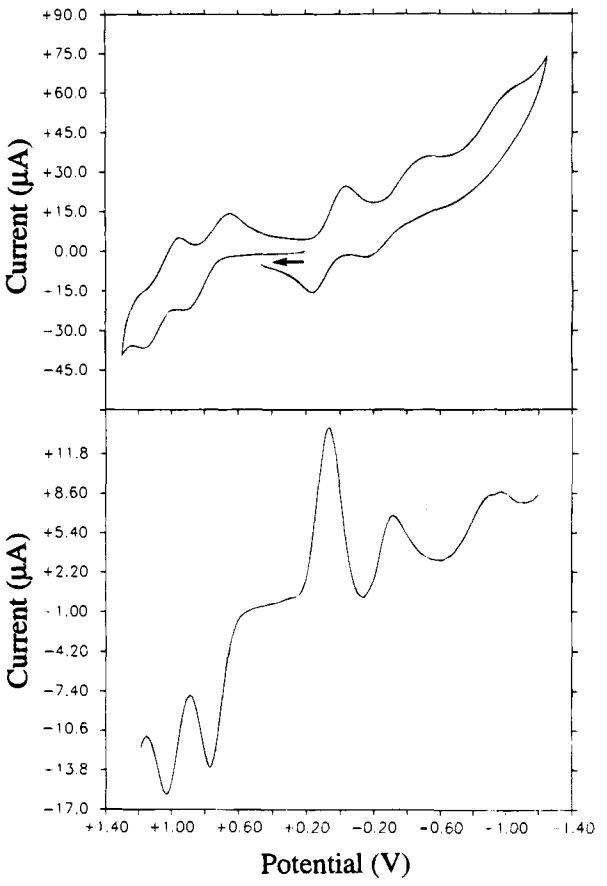

Figure 1. Cyclic voltammogram (top) and differential pulse voltammogram (bottom) of a 1 mM CH_2Cl_2 solution of $[Mn_{12}O_{12}(O_2CEt)_{16}(H_2O)_3]$ containing 0.1 M $(NBu^n_4)(PF_6)$. The potentials are given versus the ferrocene/ferrocenium couple measured under the same conditions.

common solvent. The sensitivity of the redox potentials to the identity of the carboxylate is nevertheless a matter of some interest to us, and we have therefore addressed this point in detail. Thus, the electrochemical properties of a series of $[Mn_{12}O_{12}(O_2CR)_{16}(H_2O)_4]$ complexes (R is CH_2CH_3, C_6H_5, p-C_6H_4Cl, p-C_6H_4F, p-$C_6H_4NO_2$, p-$C_6H_4OCH_3$, p-$C_6H_4CH_2CH_3$, p-$C_6H_4CF_3$, p-$C_6H_4C_6H_5$, or 3,5-$C_6H_3Cl_2$) were examined in CH_2Cl_2 solution.

The cyclic voltammogram (CV) and differential pulse voltammogram (DPV) of complex **3** are shown in Figure 1 and are typical for this family of complexes. There are a quasireversible reduction at 0.02 V and two irreversible reductions at −0.50 and −0.85 V. Complex **3** also shows a quasireversible oxidation wave at 0.79 V and a second oxidation at 1.03 V. The peak separations of the quasireversible reduction wave at 0.02 and the 0.79 V oxidation wave are both relatively large (300 and 200 mV, respectively). A study of the scan rate (ν) dependence for the 0.02 V reduction wave showed a linear dependence of peak current with respect to $\nu^{1/2}$, which indicates that this reduction is a diffusion-controlled process. Similar potentials and reversibility are seen in CH_3CN, but the peaks are somewhat broader.

Cyclic voltammograms and differential pulse voltammograms of the nine substituted benzoates were performed under identical conditions. All complexes exhibited both the first oxidation and the first reduction waves seen for the propionate and acetate complexes; however, the presence of the second oxidation and the second and third reduction waves depended upon the particular ligand. All of the data are summarized in Table 2, where values are listed only for well-defined peaks in the DPV. It can be seen that the potentials of the first oxidation and first reduction waves vary remarkably in response to the electronic properties of the carboxylate. The $E_{1/2}$ for the reduction varies from 0.47 V *vs* ferricenium/ferrocene for the p-$C_6H_4NO_2$ substituent to 0.00 V for the R = p-$C_6H_4OCH_3$ complex. The potential of the first oxidation varies from 1.07 V for R = p-$C_6H_4CF_3$ to 0.70 V for R = p-$C_6H_4OCH_3$ and p-$C_6H_4CH_2CH_3$. As expected, $E_{1/2}$ for either process increases with the electron-withdrawing ability of the para substituent on the benzoate ring. An electron-withdrawing substituent causes the carboxylate to become less basic, reducing the electron density on the metal cluster and thereby making the cluster easier to reduce and concomitantly harder to oxidize. A plot of $E_{1/2}$ vs the Hammett σ_p constants for the substituted benzoates is relatively linear, providing a quantitative measure of this relationship: for the oxidations, the origin is 0.80 V and the slope is 0.41 V/σ_p ($r^2 = 0.83$); for the reductions, the origin is 0.11 V and the slope is 0.49 V/σ_p ($r^2 = 0.94$), where the origin is the potential at $\sigma_p = 0$.

Preparation of Reduced Mn_{12} Complexes. The observation of quasireversible oxidation and reduction processes suggested that the $[Mn_{12}O_{12}(O_2CR)_{16}(H_2O)_4]$ complexes might be attainable for study at a second oxidation level, and investigations along these lines were initiated. The oxidation processes in Table 2 are at rather high potentials, but the reduction processes are much more accessible, and it was therefore decided to initially seek isolation of one-electron reduced species. The reducing agent chosen was I^- because of its sufficient, yet mild reducing strength, its ready availability as a variety of salts of organic cations, and the high solubility of many of the latter in organic solvents. Indeed, chemical reduction of the complexes $[Mn_{12}O_{12}(O_2CPh)_{16}(H_2O)_4]$ (**2**) and $[Mn_{12}O_{12}(O_2CEt)_{16}(H_2O)_4]$ (**3**) with C^+I^- (C^+ is $NPr^n_4^+$, PPh_4^+, or PPN^+) in MeCN or CH_2Cl_2 was found to provide a convenient route to the corresponding salts of the anions $[Mn_{12}O_{12}(O_2CPh)_{16}(H_2O)_4]^-$ and $[Mn_{12}O_{12}(O_2CEt)_{16}(H_2O)_4]^-$ in good (>50%) yield. The C^+I^- reagent provides the required cation, and the only byproduct is elemental I_2, which is easy to remove (eq 1). The

$$[Mn_{12}] + C^+I^- \rightarrow (C^+)[Mn_{12}]^- + {}^1/_2I_2 \qquad (1)$$

products are easily isolated as microcrystalline solids, and their formulations as $(PPh_4)[Mn_{12}O_{12}(O_2CEt)_{16}(H_2O)_4]$ (**4**), $(NPr^n_4)[Mn_{12}O_{12}(O_2CPh)_{16}(H_2O)_4]\cdot H_2O$ (**5**), $(PPh_4)[Mn_{12}O_{12}(O_2CPh)_{16}(H_2O)_4]\cdot 2H_2O$ (**6**), and $(PPN)[Mn_{12}O_{12}(O_2CPh)_{16}(H_2O)_4]$ (**7**) are supported by elemental analyses, IR and NMR (*vide infra*) spectroscopies, and conductivity measurements in MeCN and CH_2Cl_2 that indicate 1:1 electrolytes. All of the $[Mn_{12}O_{12}(O_2CR)_{16}(H_2O)_4]^{0/-}$ complexes exhibit five characteristic peaks in the 500−700 cm^{-1} region of the IR spectrum. These infrared stretches shift somewhat in response to changes in the carboxylate substituent. The approximate positions of the peaks are 670, 650, 615, 550, and 520 cm^{-1} and are apparently attributable to Mn−oxo stretches of the core.

X-ray Structure of $[Mn_{12}O_{12}(O_2CEt)_{16}(H_2O)_3]\cdot 4H_2O$ ($3\cdot 4H_2O$). The complex crystallizes in the triclinic $P\bar{1}$ space group with two molecules in the unit cell, related by a crystallographic center of inversion. Figure 2 shows an ORTEP plot with propionate methyl groups omitted for clarity, and a stereoview of the unit cell with solvate molecules omitted for clarity. Selected bond distances and bond angles are given in Tables 3 and 4, respectively.

The structure of complex $3\cdot 4H_2O$ is quite similar in many respects to the previously characterized complexes **1** and **2**. There is a central Mn_4O_4 cubane moiety, surrounded by a nonplanar ring of eight Mn atoms which are bridged by and

Table 2. Electrochemical Data[a] for $[Mn_{12}O_{12}(O_2CR)_{16}(H_2O)_4]$ Complexes in CH_2Cl_2

R	$E_{1/2}$ (1st reduction)	$E_{1/2}$ (2nd reduction)	$E_{1/2}$ (1st oxidation)	$E_{1/2}$ (2nd oxidation)
CH_2CH_3	0.02	−0.50	0.79	1.03
C_6H_5	0.12	−0.23	0.82	1.16
$C_6H_4OCH_3$	0.00		0.70	1.00
$C_6H_4CH_2CH_3$	0.02		0.70	
$C_6H_3Cl_2$	0.04			
$C_6H_4C_6H_5$	0.10		0.79	1.12
C_6H_4F	0.23	−0.10	0.93	1.18
C_6H_4Cl	0.30	−0.03	0.97	1.22
$C_6H_4CF_3$	0.35		1.07	
$C_6H_4NO_2$	0.47	0.22	1.05	

[a] Potentials were obtained from the DPV scans and are given in volts vs the ferrocene/ferrocenium couple. Only those couples that gave well-resolved features in the DPV scans are included.

connected to the cube via μ_3-O^{2-} ions. A total of 16 propionates bridge the outer-ring Mn atoms to both the inner core and the other outer-ring Mn atoms. Charge considerations indicate a $Mn^{III}_8Mn^{IV}_4$ composition. The Mn−O bond distances (Table 3) make it clear that all of the atoms in the central cube are Mn^{IV}, while the ring consists of eight Mn^{III} atoms. These assignments are supported by the marked Jahn−Teller elongation of the axial Mn−O propionate bonds (2.133−2.218 Å), which are on average 0.216 Å longer than the analogous equatorial Mn−O bonds (1.908−1.974 Å).

Compared to the other structurally characterized $[Mn_{12}O_{12}]$ compounds, complex **3**·$4H_2O$ has one interesting feature. Unlike complexes **1** and **2**, **3**·$4H_2O$ has only three bound H_2O ligands, Mn(8) being five coordinate. Although this was somewhat surprising given the presence of four H_2O ligands in **1** and **2**, there is precedence[18] for the presence of five-coordinate Mn atoms in polynuclear Mn complexes consisting predominantly of six-coordinate Mn atoms. Since water exchange is quite facile in solution (*vide infra*), it is not surprising that although four water molecules are present in the crystal lattice, one Mn remains five coordinate. It is not expected that Mn(8) would remain five coordinate in solution, however (*vide infra*).

X-ray Structure of $(PPh_4)[Mn_{12}O_{12}(O_2CEt)_{16}(H_2O)_4]$ (4). This complex crystallizes in the space group $P2_1/c$. An ORTEP plot of the anion of **4** and a stereoview of the unit cell are shown in Figure 3. Selected bond distances and angles are given in Tables 5 and 6, respectively. The successful attainment of the crystal structure allowed us to address (i) whether the reaction with I^- truly gives a stable one-electron reduced version of **3** with little or no change to the $[Mn_{12}O_{12}]$ core topology, and (ii) if the complex is indeed reduced, where the added electron resides. Crystallographic confirmation of the 1:1 cation:anion ratio and a cursory glance at Figure 3 indicates the answer to question (i) is affirmative. A closer inspection of Figure 3 and its metric parameters in Tables 5 and 6 serve to identify the recipient of the added electron as an outer (formerly Mn^{III}) ion rather than an inner, cubane Mn^{IV} ion. Thus, one outer-ring Mn^{III} has been converted to Mn^{II}. The evidence for this is discussed below, together with a rationalization of the counterintuitive, preferential reduction of a Mn^{III} ion rather than a Mn^{IV} ion.

A comparison of average metric parameters for all four structurally characterized $[Mn_{12}O_{12}]$ complexes is given in Table 7. The shape and volume of the inner $[Mn^{IV}_4O_4]$ cube remains essentially constant for all of the complexes, including the one-electron reduced complex **4**. In fact, everything looks very similar in all four complexes except for the Mn(10) atom in complex **4**. For this atom, the equatorial Mn−oxide and Mn−carboxylate oxygen bond lengths show a pronounced elongation (2.06−2.17 Å) relative to the corresponding bond distances (1.86−1.99 Å) for the Mn(10) atoms in complexes **1**, **2**, and **3**·$4H_2O$. Clearly, the Mn(10) atom in complex **4** is a Mn^{II} ion, and it does *not* exhibit a Jahn−Teller distortion as seen for all the Mn^{III} ions in the former complexes. Complex **4** is thus a very unusual example of a complex containing the same metal in three oxidation levels and it is only the second example of a complex with valence-trapped Mn^{II}, Mn^{III}, and Mn^{IV} ions in the same molecule. The only other example is a linear tetranuclear complex possessing two outer Mn^{II} ions and an inner $Mn^{III}Mn^{IV}$ pair, the latter being disordered crystallographically.[19] In fact, the oxidation state assignment for this tetranuclear complex, which is not resolved by the X-ray structure, was determined by EPR experiments.

It is possible to rationalize why a Mn^{III} ion, rather than a core Mn^{IV} ion, is reduced to a Mn^{II} ion in complex **4**. For a Mn^{IV} ion to become reduced it would have to undergo significant structural rearrangement because a Jahn−Teller distortion is expected for high-spin Mn^{III} (d^4). However, a Jahn−Teller distorted Mn^{III} ion in the cubane core would create strain in the apparently rigid $[Mn_4O_4]$ unit. In contrast, with the electron trapped on an outer Mn atom of the ring, where the bonding framework is less rigid, the additional equatorial elongation on one outer Mn atom would *not* perturb the basic $[Mn_{12}O_{12}]$ structure significantly. It should be noted that for polynuclear mixed-valence Mn complexes in the solid state a valence-trapped electronic structure is the rule. The relatively large Jahn−Teller distortion of the Mn^{III} ion is probably the origin of this observation. There is only one triangular μ_3-oxo-bridged $Mn^{II}Mn^{III}_2$ complex that has been shown[20] to become valence detrapped. In this case there are appreciable intermolecular interactions that serve to modulate dynamically the potential-energy ground-state surface of this $Mn^{II}Mn^{III}_2$ complex.

A bond valence sum analysis was carried out on complexes **3**·$4H_2O$ and **4** in order to gain further evidence for the described oxidation state assignment in complex **4**. A bond valence sum[21] is an empirical value, based on crystallographically determined metal−ligand bond distances, that may be used to calculate the oxidation state of a metal. Bond valence sums(s) are calculated using eq 2, where r is the observed bond length, and r_o and B

$$s = \exp[(r_o - r)/B] \quad (2)$$

are empirically determined parameters. Values for r_o are tabulated for Mn^{n+} (n = 2, 3, 4). Bond sum analysis has been used to verify oxidation states in metalloenzymes and super-

(18) (a) Wang, S.; Huffman, J. C.; Folting, K.; Streib, W. E.; Lobkovsky, E. B.; Christou, G. *Angew. Chem., Int. Ed. Engl.* **1991**, *30*, 1672. (b) Vincent, J. B.; Christmas, C.; Chang, H.-R.; Li, Q.; Boyd, P. D. W.; Huffman, J. C.; Hendrickson, D. N.; Christou, G. *J. Am. Chem. Soc.* **1989**, *111*, 2086.

(19) Chan, M. K.; Armstrong, W. H. *J. Am. Chem. Soc.* **1990**, *112*, 4985.

(20) Jang, H. G.; Vincent, J. B.; Nakano, M.; Huffman, J. C.; Christou, G.; Sorai, M.; Wittebort, R. J.; Hendrickson, D. N. *J. Am. Chem. Soc.* **1989**, *111*, 7778.

(21) Brown, I. D.; Altermatt, D. *Acta Crystallogr. Sect. B* **1985**, *41*, 244.

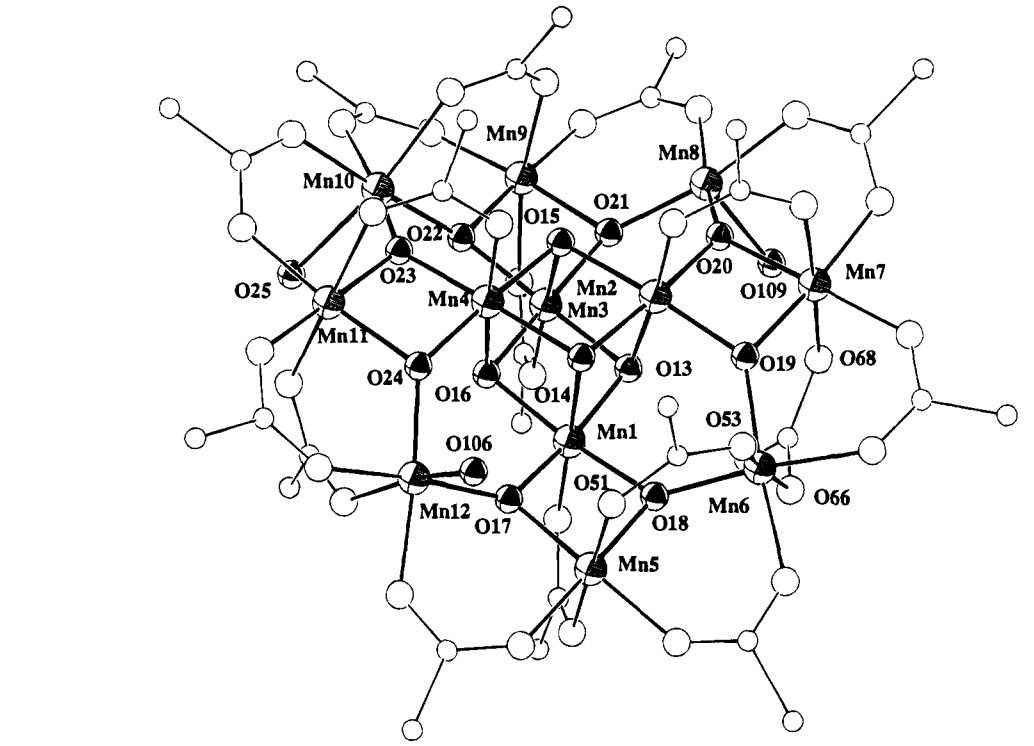

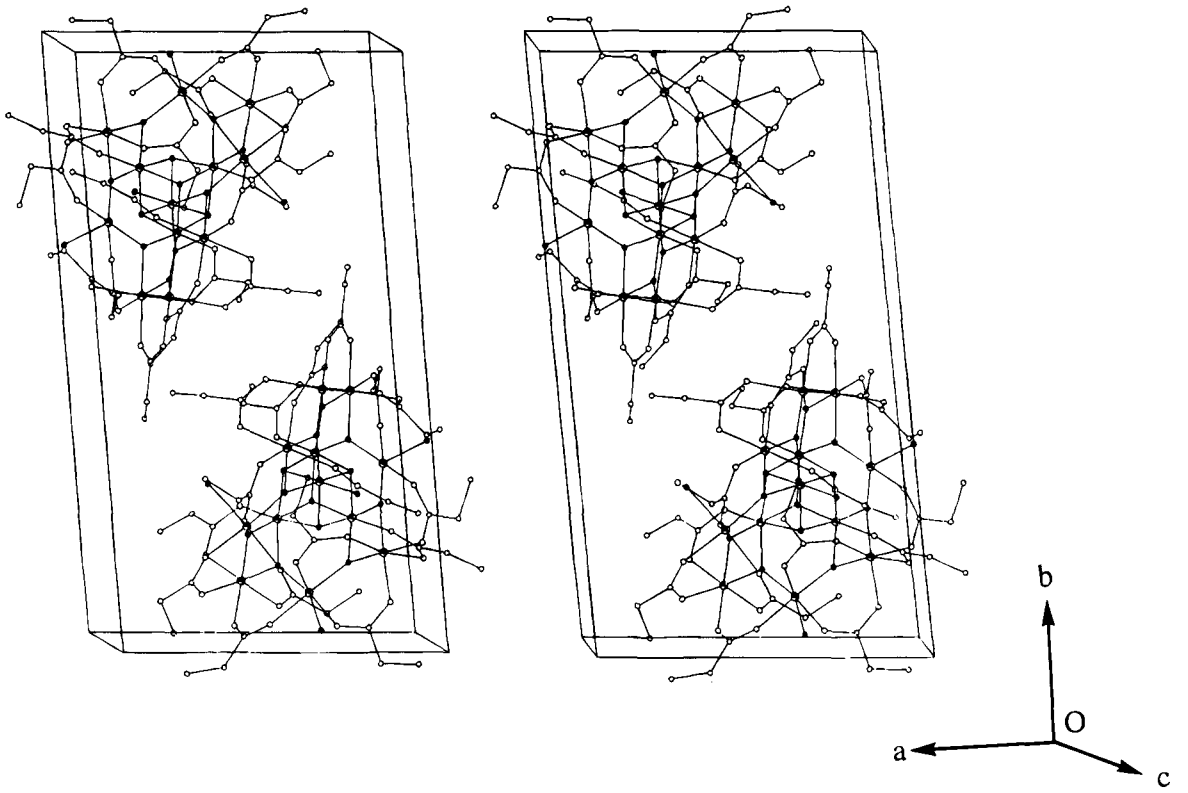

Figure 2. ORTEP representations of $[Mn_{12}O_{12}(O_2CEt)_{16}(H_2O)_3]\cdot 4H_2O$ ($\mathbf{3}\cdot 4H_2O$) at the 50% probability level (top). The methyl groups of the propionate ligands and the H_2O solvate molecules are omitted for clarity. To avoid congestion, only the $[Mn_{12}O_{12}(H_2O)_3]$ core atoms are labeled plus O(106), O(51), O(52), O(66), O(68), and O(109), which are referred to in the text. At the bottom is a stereoview of the unit cell showing the disposition of the Mn_{12} molecules about the inversion center at ($^1/_2$,$^1/_2$,$^1/_2$).

conductors,[22] as well as in the only other compound proposed to have Mn^{II}, Mn^{III}, and Mn^{IV} in the same molecule.[23]

As can be seen in Table 8, bond valence sums for the two complexes also indicate that the extra electron in the reduced species resides only on Mn(10), at least in the solid state at −168 °C. Note that even the five-coordinate Mn(8) atom in the neutral complex **3** provides a bond valence sum expected for a Mn^{III} center. The bond valence sum averaged over the

(22) Brown, I. D. *Solid State Chem.* **1989**, *82*, 122.

(23) Thorpe, H. H. *Inorg. Chem.* **1992**, *31*, 1585.

Table 3. Selected[a] Interatomic Distances for $[Mn_{12}O_{12}(O_2CEt)_{16}(H_2O)_3]\cdot 4H_2O$ (**3**·4H_2O)

A	B	distance (Å)	A	B	distance (Å)
Mn(1)	Mn(2)	2.819(2)	Mn(4)	O(14)	1.910(5)
Mn(1)	Mn(3)	2.926(2)	Mn(4)	O(15)	1.917(5)
Mn(1)	Mn(4)	2.832(2)	Mn(4)	O(16)	1.909(5)
Mn(1)	Mn(5)	2.765(2)	Mn(4)	O(23)	1.843(5)
Mn(1)	Mn(6)	3.431(2)	Mn(4)	O(24)	1.856(4)
Mn(1)	Mn(12)	3.435(2)	Mn(5)	Mn(6)	3.393(2)
Mn(1)	O(13)	1.920(5)	Mn(5)	Mn(12)	3.387(2)
Mn(1)	O(14)	1.911(5)	Mn(5)	O(17)	1.898(5)
Mn(1)	O(16)	1.907(5)	Mn(5)	O(18)	1.899(5)
Mn(1)	O(17)	1.845(5)	Mn(6)	Mn(7)	3.411(2)
Mn(1)	O(18)	1.860(5)	Mn(6)	O(18)	1.880(5)
Mn(2)	Mn(3)	2.828(2)	Mn(6)	O(19)	1.900(5)
Mn(2)	Mn(4)	2.900(2)	Mn(7)	Mn(8)	3.333(2)
Mn(2)	Mn(7)	2.764(2)	Mn(7)	O(19)	1.894(5)
Mn(2)	Mn(6)	3.437(2)	Mn(7)	O(20)	1.892(5)
Mn(2)	Mn(8)	3.437(2)	Mn(8)	Mn(9)	3.341(2)
Mn(2)	O(13)	1.905(5)	Mn(8)	O(20)	1.859(5)
Mn(2)	O(14)	1.897(5)	Mn(8)	O(21)	1.874(5)
Mn(2)	O(15)	1.920(5)	Mn(8)	O(109)	2.107(6)
Mn(2)	O(19)	1.866(5)	Mn(9)	Mn(10)	3.305(2)
Mn(2)	O(20)	1.863(5)	Mn(9)	O(21)	1.914(5)
Mn(3)	Mn(4)	2.833(2)	Mn(9)	O(22)	1.874(5)
Mn(3)	Mn(9)	2.765(2)	Mn(10)	Mn(11)	3.414(2)
Mn(3)	Mn(8)	3.446(2)	Mn(10)	O(22)	1.910(5)
Mn(3)	Mn(10)	3.464(2)	Mn(10)	O(23)	1.878(5)
Mn(3)	O(13)	1.904(5)	Mn(10)	O(25)	2.175(5)
Mn(3)	O(15)	1.890(5)	Mn(11)	Mn(12)	3.335(2)
Mn(3)	O(16)	1.911(5)	Mn(11)	O(23)	1.892(5)
Mn(3)	O(21)	1.876(5)	Mn(11)	O(24)	1.912(5)
Mn(3)	O(22)	1.881(5)	Mn(12)	O(17)	1.885(5)
Mn(4)	Mn(11)	2.760(2)	Mn(12)	O(24)	1.882(5)
Mn(4)	Mn(10)	3.423(2)	Mn(12)	O(106)	2.184(5)
Mn(4)	Mn(12)	3.426(2)			

[a] For the $[Mn_{12}O_{12}]$ core and H_2O molecules only; a full listing is available in the supplementary material.

whole cluster shows a distinct decrease for **4** compared with **3**, as expected upon reduction. In general, all calculated bond valence sum values are slightly high for higher valent Mn atoms (III and IV) because of the ability of oxo ligands to contribute some π-bonding component to the Mn−oxo bond, thus resulting in a shorter bond length.

Since the above structure for complex **4** showing the added electron to be trapped on Mn(10) was obtained at −168 °C, it was decided to determine the structure from a higher temperature data set to examine whether the extra electron would detrap and result in Mn(10) no longer being distinct from the other outer Mn atoms. Data collection on a crystal of **4** at 20 °C yielded considerably poorer quality data then those obtained at −168 °C. There was no change in space group; the details of the X-ray structural analysis with the 20 °C data set are available in the supplementary material. In Table 9 is given a comparison of selected average bond distances from the −168 and 20 °C crystal structures of complex **4**. It is clear that even at 20 °C the extra electron remains on the Mn(10) atom in the solid state.

^{1}H NMR Spectroscopy. An ^{1}H NMR (300 MHz) study of complexes **1**, **3**, and **4** was carried out in order to probe their structure in solution. The ^{1}H NMR spectrum of a CD_3CN solution of $[Mn_{12}O_{12}(O_2CMe)_{16}(H_2O)_4]$ (**1**) exhibits four peaks at δ = 13.9, 18.7, 41.8, and 48.2 ppm (see Table 10). The peak at δ = 18.7 ppm is significantly broader than the other three peaks. The other three peaks (two downfield and one upfield) are not evident when CD_3CO_2D is used in the preparation of the complex instead of $MeCO_2H$ and show a 1:2:1 intensity pattern indicating that there are only three magnetically distinguishable types of acetates in the complex. No free H_2O peak is evident in the spectrum and hence the very broad peak at δ = 18.7 ppm is assigned as a weighted average of the

Table 4. Selected[a] Angles for $[Mn_{12}O_{12}(O_2CEt)_{16}(H_2O)_3]\cdot 4H_2O$ (**3**·4H_2O)

A	B	C	angle (deg)	A	B	C	angle (deg)
O(13)	Mn(1)	O(14)	83.52(20)	O(21)	Mn(8)	O(109)	95.21(23)
O(13)	Mn(1)	O(16)	79.80(21)	O(21)	Mn(9)	O(22)	84.38(20)
O(13)	Mn(1)	O(17)	172.43(23)	O(22)	Mn(10)	O(23)	93.03(21)
O(13)	Mn(1)	O(18)	97.50(21)	O(22)	Mn(10)	O(25)	93.00(20)
O(14)	Mn(1)	O(16)	83.49(21)	O(23)	Mn(11)	O(24)	82.97(20)
O(14)	Mn(1)	O(17)	89.56(21)	O(17)	Mn(12)	O(24)	93.77(21)
O(14)	Mn(1)	O(18)	90.06(22)	O(24)	Mn(12)	O(106)	93.89(20)
O(16)	Mn(1)	O(17)	96.41(21)	Mn(2)	O(13)	Mn(3)	95.88(23)
O(16)	Mn(1)	O(18)	173.23(22)	Mn(1)	O(13)	Mn(3)	99.87(22)
O(17)	Mn(1)	O(18)	85.53(22)	Mn(1)	O(13)	Mn(2)	94.97(21)
O(13)	Mn(2)	O(14)	84.32(20)	Mn(1)	O(14)	Mn(2)	95.53(21)
O(13)	Mn(2)	O(15)	83.04(21)	Mn(1)	O(14)	Mn(4)	95.63(22)
O(13)	Mn(2)	O(19)	90.25(22)	Mn(2)	O(14)	Mn(4)	99.25(23)
O(13)	Mn(2)	O(20)	91.22(21)	Mn(2)	O(15)	Mn(3)	95.84(22)
O(14)	Mn(2)	O(15)	81.32(20)	Mn(2)	O(15)	Mn(4)	98.22(22)
O(14)	Mn(2)	O(19)	98.72(21)	Mn(3)	O(15)	Mn(4)	96.18(21)
O(14)	Mn(2)	O(20)	173.96(22)	Mn(1)	O(16)	Mn(3)	100.11(22)
O(15)	Mn(2)	O(19)	173.27(22)	Mn(1)	O(16)	Mn(4)	95.82(21)
O(15)	Mn(2)	O(20)	94.13(21)	Mn(3)	O(16)	Mn(4)	95.74(21)
O(19)	Mn(2)	O(20)	85.33(21)	Mn(1)	O(17)	Mn(5)	95.24(22)
O(13)	Mn(3)	O(15)	83.87(21)	Mn(1)	O(17)	Mn(12)	134.1(3)
O(13)	Mn(3)	O(16)	80.10(20)	Mn(5)	O(17)	Mn(12)	127.15(26)
O(13)	Mn(3)	O(21)	96.63(21)	Mn(1)	O(18)	Mn(5)	94.71(23)
O(13)	Mn(3)	O(22)	174.17(21)	Mn(1)	O(18)	Mn(6)	133.05(28)
O(15)	Mn(3)	O(16)	83.61(20)	Mn(5)	O(18)	Mn(6)	127.7(3)
O(15)	Mn(3)	O(21)	90.37(20)	Mn(2)	O(19)	Mn(6)	131.77(26)
O(15)	Mn(3)	O(22)	90.61(21)	Mn(2)	O(19)	Mn(7)	94.65(23)
O(16)	Mn(3)	O(21)	173.41(21)	Mn(6)	O(19)	Mn(7)	128.1(3)
O(16)	Mn(3)	O(22)	97.47(21)	Mn(2)	O(20)	Mn(7)	94.82(22)
O(21)	Mn(3)	O(22)	85.23(21)	Mn(2)	O(20)	Mn(8)	134.95(27)
O(14)	Mn(4)	O(15)	81.06(20)	Mn(7)	O(20)	Mn(8)	125.45(26)
O(14)	Mn(4)	O(16)	83.43(21)	Mn(3)	O(21)	Mn(8)	133.54(27)
O(14)	Mn(4)	O(23)	173.14(21)	Mn(3)	O(21)	Mn(9)	93.69(21)
O(14)	Mn(4)	O(24)	96.78(21)	Mn(8)	O(21)	Mn(9)	123.77(27)
O(15)	Mn(4)	O(16)	82.93(20)	Mn(3)	O(22)	Mn(9)	94.84(21)
O(15)	Mn(4)	O(23)	95.77(20)	Mn(3)	O(22)	Mn(10)	132.03(26)
O(15)	Mn(4)	O(24)	174.83(21)	Mn(9)	O(22)	Mn(10)	121.72(25)
O(16)	Mn(4)	O(23)	90.17(21)	Mn(4)	O(23)	Mn(10)	133.76(25)
O(16)	Mn(4)	O(24)	92.18(20)	Mn(4)	O(23)	Mn(11)	95.27(22)
O(23)	Mn(4)	O(24)	85.88(21)	Mn(10)	O(23)	Mn(11)	129.77(26)
O(17)	Mn(5)	O(18)	83.01(22)	Mn(4)	O(24)	Mn(11)	94.20(22)
O(18)	Mn(6)	O(19)	94.81(22)	Mn(4)	O(24)	Mn(12)	132.85(27)
O(19)	Mn(7)	O(20)	83.74(21)	Mn(11)	O(24)	Mn(12)	123.03(24)
O(20)	Mn(8)	O(21)	93.68(21)				

[a] For the $[Mn_{12}O_{12}(H_2O)_3]$ core only; a full listing is available in supplementary material.

coordinated H_2O and the free H_2O (the crystals are hydrated and there is water in the solvent). Both the broadness of this peak and its chemical shift are highly dependent on the concentration of the complex in solution; as the concentration of the complex in solution is increased, the peak becomes broader and is more paramagnetically shifted downfield, consistent with the ratio of coordinated H_2O to free H_2O increasing as the concentration of the complex in solution is increased. It is clear that the water exchange rate is fast on the ^{1}H NMR time scale, a behavior consistent with H_2O ligands coordinated to labile Mn^{III} ions.

Because the 16 carboxylate ligands of complex **1** give only three signals in solution, the S_4 symmetry of complex **1** in the solid state, which would afford four types of carboxylate environments, appears to be maintained in solution. In addition, to account for the doubly intense peak, two of the carboxylates must be similar enough magnetically that they result in coincidentally overlapping peaks; this supposition is further supported by the NMR spectrum of complex **3** (*vide infra*). Two of the acetate peaks are located much further downfield with relatively similar chemical shifts, while one peak is located much closer to the diamagnetic region. This indicates that the two downfield peaks are more closely related magnetically. If this is the case, the 3:1 ratio of the downfield signals to the upfield

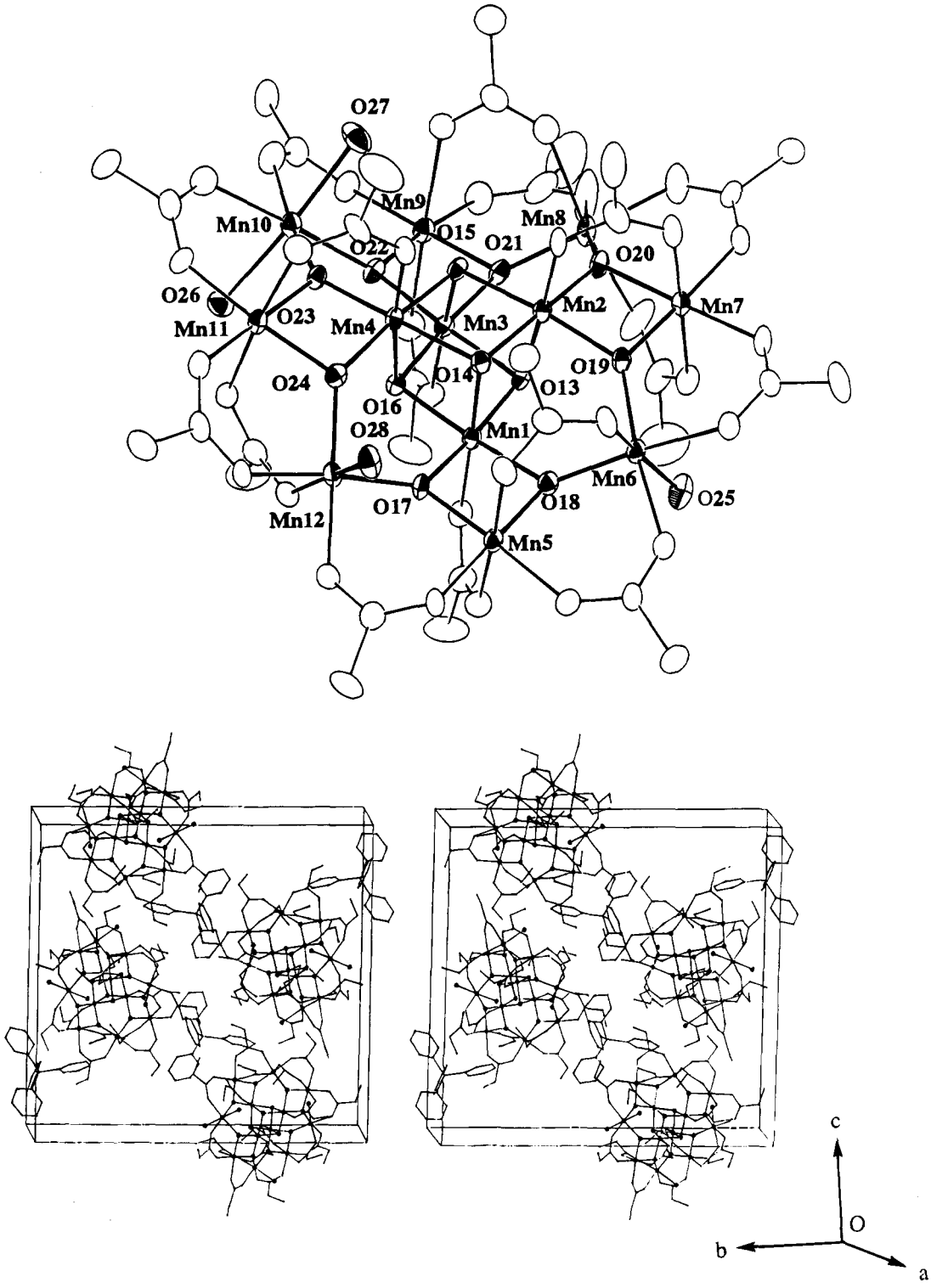

Figure 3. ORTEP representation of the anion of $(PPh_4)[Mn_{12}O_{12}(O_2CEt)_{16}(H_2O)_4]$ (**4**) at the 50% probability level (top). The methyl groups of the propionate ligands are omitted for clarity. To avoid congestion, only the $[Mn_{12}O_{12}(H_2O)_4]$ core atoms are labeled. At the bottom is a stereoview of the unit cell with solvent molecules omitted for clarity.

signal suggests that the upfield signal is from the four acetates that bridge the four $Mn^{III}\cdots Mn^{IV}$ pairs, while the other two signals are from the 12 acetate groups that bridge the eight $Mn^{III}\cdots Mn^{III}$ pairs. In addition, the doubly intense signal can be tentatively assigned to the eight equatorial acetates, which would not be expected to have significantly different magnetic environments, especially in solution where the outer ring would be more flexible. By process of elimination, the furthermost downfield peak is therefore assigned to the Jahn–Teller elongated axial carboxylates. The assignments for all of the peaks observed for complex **1** are collected in Table 10.

In addition to coordinated H_2O exchange, other more interesting issues of dynamics surface from an examination of the ^1H NMR spectra of the propionate complexes **3** and **4** shown in Figure 4. The increased solubility of complex **3** makes it possible to obtain spectra in various solvents. ^1H NMR spectra of complex **3** in toluene-d_8 and CD_3CN are very similar, with only minor differences in the positions of several peaks (see

Table 5. Selected[a] Interatomic Distances for $(PPh_4)[Mn_{12}O_{12}(O_2CEt)_{16}(H_2O)_4]$ (**4**)

A	B	distance (Å)	A	B	distance (Å)
Mn(1)	Mn(2)	2.806(1)	Mn(4)	O(14)	1.945(5)
Mn(1)	Mn(3)	2.954(1)	Mn(4)	O(15)	1.938(6)
Mn(1)	Mn(4)	2.828(1)	Mn(4)	O(16)	1.899(5)
Mn(1)	Mn(5)	2.774(1)	Mn(4)	O(23)	1.821(5)
Mn(1)	Mn(6)	3.466(1)	Mn(4)	O(24)	1.880(6)
Mn(1)	Mn(12)	3.433(1)	Mn(5)	Mn(6)	3.331(1)
Mn(1)	O(13)	1.896(5)	Mn(5)	Mn(12)	3.390(1)
Mn(1)	O(14)	1.894(5)	Mn(5)	O(17)	1.869(5)
Mn(1)	O(16)	1.920(5)	Mn(5)	O(18)	1.902(6)
Mn(1)	O(17)	1.861(5)	Mn(6)	O(18)	1.884(6)
Mn(1)	O(18)	1.897(5)	Mn(6)	O(19)	1.890(5)
Mn(2)	Mn(3)	2.848(1)	Mn(6)	O(25)	2.208(6)
Mn(2)	Mn(4)	2.955(1)	Mn(7)	Mn(8)	3.381(1)
Mn(2)	Mn(7)	2.770(1)	Mn(7)	O(19)	1.880(6)
Mn(2)	Mn(6)	3.446(1)	Mn(7)	O(20)	1.898(5)
Mn(2)	Mn(8)	3.459(1)	Mn(8)	Mn(9)	3.362(1)
Mn(2)	O(13)	1.899(5)	Mn(8)	O(20)	1.910(6)
Mn(2)	O(14)	1.903(5)	Mn(8)	O(21)	1.892(6)
Mn(2)	O(15)	1.922(5)	Mn(9)	Mn(10)	3.517(1)
Mn(2)	O(19)	1.871(5)	Mn(9)	O(21)	1.906(5)
Mn(2)	O(20)	1.864(6)	Mn(9)	O(22)	1.877(6)
Mn(3)	Mn(4)	2.862(2)	Mn(10)	Mn(11)	3.516(1)
Mn(3)	Mn(9)	2.749(2)	Mn(10)	O(22)	2.097(5)
Mn(3)	Mn(8)	3.451(1)	Mn(10)	O(23)	2.064(5)
Mn(3)	Mn(10)	3.604(1)	Mn(10)	O(26)	2.195(6)
Mn(3)	O(13)	1.967(5)	Mn(10)	O(27)	2.238(6)
Mn(3)	O(15)	1.918(5)	Mn(11)	Mn(12)	3.334(5)
Mn(3)	O(16)	1.942(5)	Mn(11)	O(23)	1.864(5)
Mn(3)	O(21)	1.858(6)	Mn(11)	O(24)	1.910(5)
Mn(3)	O(22)	1.836(5)	Mn(12)	O(17)	1.878(5)
Mn(4)	Mn(11)	2.753(2)	Mn(12)	O(24)	1.897(5)
Mn(4)	Mn(10)	3.577(1)	Mn(12)	O(28)	2.208(6)
Mn(4)	Mn(12)	3.447(1)			

[a] For the $[Mn_{12}O_{12}]$ core and H_2O molecules only; a full listing is available in the supplementary material.

Table 10). The chemical shift and broadness of the H_2O peak also varies with concentration in toluene solution.

The spectrum for complex **3** (Figure 4, top) shows only a total of seven carboxylate peaks. This indicates that the effective solution symmetry is higher than the solid-state symmetry (C_1). Intramolecular carboxylate exchange can be envisioned, especially between the axial water and carboxylate sites. However, exchange with free propionic acid in solution is not fast relative to the ^1H NMR time scale, because an unwashed sample showed separate, sharp peaks for the free carboxylic acid. The seven peaks for complex **3** can be assigned through analogy with the ^1H NMR spectrum of complex **1** and through peak integration to differentiate the CH_2 and CH_3 groups. Using these methods, the four carboxylate peaks furthermost downfield are assigned to CH_2 groups and the remaining peaks to CH_3 groups; a smaller paramagnetic shift is consistent with the increased distance of the CH_3 groups from the paramagnetic center, relative to the CH_2 groups.

Spin–lattice relaxation times (T_1), measured using the inversion recovery method, of the ^1H NMR peaks of complex **3** were performed in order to support the peaks assignments. In general, longitudinal relaxation time is directly related to the distance of a proton from the paramagnetic center (*e.g.* for a propionate complex, the CH_3 proton resonance should have a longer T_1 than the CH_2 proton, which is closer to the metal center). However, it was also hoped that through a study of T_1 values as well as other supporting NMR data, a particular CH_2 group could be paired with its corresponding CH_3 group. Indeed, by comparing relative T_1 values for CH_2 and CH_3 proton resonances, the CH_2 protons with the longest T_1 values could be satisfactorily paired with the CH_3 protons with longest T_1 values. In order to confirm the assignment of the upfield CH_2 peak, T_1 values were also measured for complex **1**. Because the most upfield peak in the spectrum of complex **1** has such a long T_1 time compared to the other two CH_3 proton resonances, it provided the precedent for a significantly longer T_1 time for the most upfield CH_2 resonance in the spectrum of complex **3**. Using this method, the closely spaced CH_2 and CH_3 peaks at 12.2 and 11.1 ppm in the spectrum of complex **3** could be assigned with confidence. An additional piece of evidence for the CH_2 and CH_3 assignments came from the preparation of the 2,2-dichloropropionate complex. The NMR spectrum of this compound showed only the three peaks close to the diamagnetic region, which although somewhat shifted from their positions in the nonchlorinated propionate, confirm the assignment of the methylene groups as the four downfield peaks.

Finally, a variable-temperature NMR study of complex **3** was performed in toluene-d_8 in the temperature range of 23 °C to −58 °C. In general, as the temperature was lowered, the peaks shifted further from their diamagnetic positions, which is as expected given that the magnetic moment of the complex increases at lower temperatures (*vide infra*). In addition, at very low temperatures, the doubly intense, most upfield peak begins to split into two very broad peaks, supporting the earlier

Table 6. Selected[a] Angles for $(PPh_4)[Mn_{12}O_{12}(O_2CEt)_{16}(H_2O)_4]$ (**4**)

A	B	C	angle (deg)	A	B	C	angle (deg)
O(13)	Mn(1)	O(14)	84.17(22)	O(21)	Mn(9)	O(22)	82.82(23)
O(13)	Mn(1)	O(16)	81.35(22)	O(22)	Mn(10)	O(23)	89.01(21)
O(13)	Mn(1)	O(17)	173.08(22)	O(22)	Mn(10)	O(26)	92.74(22)
O(13)	Mn(1)	O(18)	97.60(23)	O(22)	Mn(10)	O(27)	91.33(23)
O(14)	Mn(1)	O(16)	84.28(22)	O(23)	Mn(10)	O(26)	93.97(22)
O(14)	Mn(1)	O(17)	89.36(23)	O(23)	Mn(10)	O(27)	87.04(25)
O(14)	Mn(1)	O(18)	89.80(23)	O(26)	Mn(10)	O(27)	175.82(24)
O(16)	Mn(1)	O(17)	95.59(22)	O(23)	Mn(11)	O(24)	83.41(23)
O(16)	Mn(1)	O(18)	174.06(22)	O(17)	Mn(12)	O(24)	92.17(24)
O(17)	Mn(1)	O(18)	84.81(23)	O(17)	Mn(12)	O(28)	92.87(23)
O(13)	Mn(2)	O(14)	83.85(22)	O(24)	Mn(12)	O(28)	89.41(23)
O(13)	Mn(2)	O(15)	84.60(22)	Mn(1)	O(13)	Mn(2)	95.34(23)
O(13)	Mn(2)	O(19)	90.52(22)	Mn(1)	O(13)	Mn(3)	99.76(24)
O(13)	Mn(2)	O(20)	91.69(23)	Mn(2)	O(13)	Mn(3)	94.86(22)
O(14)	Mn(2)	O(15)	80.55(23)	Mn(1)	O(14)	Mn(2)	95.28(24)
O(14)	Mn(2)	O(19)	96.54(23)	Mn(1)	O(14)	Mn(4)	94.85(23)
O(14)	Mn(2)	O(20)	175.29(23)	Mn(2)	O(14)	Mn(4)	100.36(25)
O(15)	Mn(2)	O(19)	174.54(22)	Mn(2)	O(15)	Mn(3)	95.75(23)
O(15)	Mn(2)	O(20)	97.57(23)	Mn(2)	O(15)	Mn(4)	99.95(24)
O(19)	Mn(2)	O(20)	84.97(23)	Mn(3)	O(15)	Mn(4)	95.82(24)
O(13)	Mn(3)	O(15)	82.86(22)	Mn(1)	O(16)	Mn(3)	99.82(24)
O(13)	Mn(3)	O(16)	79.00(22)	Mn(1)	O(16)	Mn(4)	95.54(23)
O(13)	Mn(3)	O(21)	94.71(23)	Mn(3)	O(16)	Mn(4)	96.32(23)
O(13)	Mn(3)	O(22)	174.54(23)	Mn(1)	O(17)	Mn(5)	96.05(24)
O(15)	Mn(3)	O(16)	82.64(23)	Mn(1)	O(17)	Mn(12)	133.3(3)
O(15)	Mn(3)	O(21)	94.23(24)	Mn(1)	O(18)	Mn(5)	93.79(24)
O(15)	Mn(3)	O(22)	91.69(23)	Mn(1)	O(18)	Mn(6)	132.9(3)
O(16)	Mn(3)	O(21)	173.25(24)	Mn(5)	O(18)	Mn(6)	123.2(3)
O(16)	Mn(3)	O(22)	100.74(24)	Mn(2)	O(19)	Mn(6)	132.8(3)
O(21)	Mn(3)	O(22)	85.28(24)	Mn(2)	O(19)	Mn(7)	95.19(25)
O(14)	Mn(4)	O(15)	79.09(22)	Mn(6)	O(19)	Mn(7)	129.1(3)
O(14)	Mn(4)	O(16)	83.47(22)	Mn(2)	O(20)	Mn(7)	94.81(25)
O(14)	Mn(4)	O(23)	175.25(24)	Mn(2)	O(20)	Mn(8)	132.8(3)
O(14)	Mn(4)	O(24)	98.26(23)	Mn(7)	O(20)	Mn(8)	125.2(3)
O(15)	Mn(4)	O(16)	83.25(22)	Mn(3)	O(21)	Mn(8)	133.9(3)
O(15)	Mn(4)	O(23)	96.96(23)	Mn(3)	O(21)	Mn(9)	93.82(25)
O(15)	Mn(4)	O(24)	174.24(23)	Mn(8)	O(21)	Mn(9)	124.5(3)
O(16)	Mn(4)	O(23)	93.48(23)	Mn(3)	O(22)	Mn(9)	95.54(25)
O(16)	Mn(4)	O(24)	91.39(23)	Mn(3)	O(22)	Mn(10)	132.7(3)
O(23)	Mn(4)	O(24)	85.43(24)	Mn(9)	O(22)	Mn(10)	124.46(28)
O(17)	Mn(5)	O(18)	84.43(23)	Mn(4)	O(23)	Mn(10)	134.0(3)
O(18)	Mn(6)	O(19)	93.86(23)	Mn(4)	O(23)	Mn(11)	96.67(25)
O(18)	Mn(6)	O(25)	91.79(24)	Mn(10)	O(23)	Mn(11)	127.0(3)
O(19)	Mn(6)	O(25)	93.76(24)	Mn(4)	O(24)	Mn(11)	93.19(24)
O(19)	Mn(7)	O(20)	83.79(24)	Mn(4)	O(24)	Mn(12)	131.8(3)
O(20)	Mn(8)	O(21)	94.57(24)	Mn(11)	O(24)	Mn(12)	122.3(3)

[a] For the $[Mn_{12}O_{12}(H_2O)_4]$ core only; a full listing is available in the supplementary material.

Table 7. Comparison of Averaged[a] Selected Structural Parameters (Å, deg) for Complexes **1**, **2**, **3**·4H$_2$O, and **4**[b]

parameter	1	2	3·4H$_2$O	4
Mn$_c$···Mn$_c$(eq)	2.943	2.991(1)	2.913(13)	2.955(1)
Mn$_c$···Mn$_c$(ax)	2.820	2.823(11)	2.828(9)	2.836(30)
Mn$_c$···Mn$_r$[c]	3.451(4)	3.457(3)	3.437(14)	3.450(17)[e] 3.591(14)[f]
Mn$_c$···Mn$_r$[d]	2.767	2.800(25)	2.764(4)	2.762(13)
Mn$_r$···Mn$_r$	3.371(60)	3.351(66)	3.365(60)	3.367(37)[e] 3.517(1)[f]
Mn$_c$–O$_c$(eq)	1.912(4)	1.933(55)	1.910(14)	1.929(38)
Mn$_c$–O$_c$(ax)	1.901	1.907(27)	1.904(14)	1.903(16)
Mn$_c$–O$_r$	1.869(15)	1.859(76)	1.861(20)	1.861(40)
Mn$_r$–O$_r$[c]	1.897(5)	1.888(41)	1.884(27)	1.892(18)[e] 2.081(17)[f]
Mn$_r$–O$_r$[d]	1.886(8)	1.902(28)	1.897(22)	1.888(24)
Mn$_r$–O$_w$	2.178	2.214(31)	2.155(48)	2.208(0)[e] 2.217(27)[f]
Mn$_c$–O$_b$	1.912	1.919(47)	1.911(3)	1.936(11)
Mn$_r$–O$_b$(eq)	1.964(47)	1.955(61)	1.950(75)	1.966(29)[e] 2.148(23)[f]
Mn$_r$–O$_b$(ax)	2.160(28)	2.176(85)	2.169(46)	2.185(78)
Mn$_c$–O$_c$–Mn$_c$(eq)	100.6	101.3(1.2)	99.4(1.1)	100.0(4)
Mn$_c$–O$_c$–Mn$_c$(ax)	95.4(1)	94.0(1.3)	95.7(7)	95.5(9)
Mn$_c$–O$_r$–Mn$_r$[c]	132.9(4)	134.7(1.7)	133.3(1.7)	133.0(1.2)
Mn$_c$–O$_r$–Mn$_r$[d]	95.0(8)	96.2(2.5)	94.7(1.0)	94.9(1.8)
Mn$_r$–O$_r$–Mn$_r$	126.1(3.0)	124.4(3.9)	125.8(4.1)	125.7(3.9)
O$_c$–Mn$_c$–O$_c$(eq)	79.3	78.7(7)	80.6(8)	80.0(1.4)
O$_c$–Mn$_c$–O$_c$(ax)	83.6(1)	84.2(1.9)	83.5(8)	83.6(1.0)
O$_r$–Mn$_c$–O$_r$	84.7	84.4(3)	85.5(4)	85.1(3)
O$_r$–Mn$_r$–O$_r$[c]	93.2	91.9(6)	93.8(1.0)	93.5(1.4)[e] 89.0[f]
O$_r$–Mn$_r$–O$_r$[d]	83.8	82.0(1.7)	83.5(9)	83.6(8)
cube volume (Å^3)[g]	7.293	7.403	7.257	7.385

[a] Averaged using the virtual D_{2d} symmetry of the $Mn_{12}O_{12}$ cores, ignoring the positioning of the water molecules. For disordered ligands, the indicated structures in the ORTEP diagrams were used. Numbers in parentheses are the greatest deviation of an individual value from the mean. Numbers without parentheses following them are single values owing to crystallographically imposed symmetry. [b] O$_c$ = central cubane oxygens; O$_r$ = outer ring oxygens; O$_w$ = water oxygens; O$_b$ = bridging carboxylate oxygens; ax = axial; eq = equatorial; Mn$_c$ = cubane Mn^{IV}; Mn$_r$ = ring Mn^{III}. [c] Mn atoms Mn (6, 8, 10, 12) in **2** and **3**·4H$_2$O; Mn atom Mn(2) in **1**. [d] Mn atoms Mn (5, 7, 9, 11) in **2** and **3**·4H$_2$O, Mn atom Mn(3) in **1**. [e] Value excluding that for unique Mn(10). [f] Value for unique Mn(10). [g] Calculated using a locally written program.

Table 8. Bond Valence Sums for Each Mn Atom in Complexes **3**·4H$_2$O and **4** Assuming Various Charges[a]

	complex **3**·4H$_2$O			complex **4**		
atom	Mn^{2+}	Mn^{3+}	Mn^{4+}	Mn^{2+}	Mn^{3+}	Mn^{4+}
Mn(1)	4.564	4.209	4.131	4.473	4.120	4.040
Mn(2)	4.535	4.184	4.106	4.428	4.110	4.034
Mn(3)	4.515	4.164	4.085	4.400	4.056	3.981
Mn(4)	4.588	4.230	4.155	4.449	4.103	4.025
Mn(5)	3.533	3.255	3.193	3.530	3.254	3.195
Mn(6)	3.509	3.235	3.175	3.443	3.175	3.115
Mn(7)	3.534	3.259	3.198	3.530	3.255	3.194
Mn(8)	3.371	3.108	3.050	3.359	3.097	3.040
Mn(9)	3.570	3.292	3.230	3.435	3.158	3.108
Mn(10)	3.485	3.215	3.154	2.308	2.129	2.090
Mn(11)	3.509	3.236	3.177	3.447	3.180	3.119
Mn(12)	3.555	3.277	3.216	3.474	3.204	3.143

[a] The underlined value is the one closest to the actual charge for which it was calculated. The oxidation state of a particular atom can be taken as the nearest whole number to the underlined value.

conclusion that this peak is due to the coincidental overlap of two CH$_3$ resonances.

The characterization of complex **4** in solution is important because the valence trapping of the additional electron in the solid state structure (which yields C_2 symmetry) may or may not lead to the observation of the effects of a unique Mn^{II} in the NMR spectrum, depending on whether there are mechanisms available that allow the interconversion of the Mn^{II} and Mn^{III} sites at a suitable rate. As can be seen in Figure 4 (bottom), the spectrum of complex **4** shows in fact a similar pattern of peaks to the neutral complex **3**. Peak positions are given in Table 10. In addition to the presence of an additional peak due to the cation, the peaks for complex **4** are shifted noticeably toward the diamagnetic region from their analogous positions in the neutral complex **3**. However, no separate peak due to a

Table 9. Comparison of Selected Average[a] Bond Distances for the −168 and 20 °C Crystal Structures of [PPh$_4$][Mn$_{12}$O$_{12}$(O$_2$CEt)$_{16}$(H$_2$O)$_4$] (**4**)[b]

bond distance	−168 °C	20 °C	Δ(20 °C − 168 °C)
Mn^{IV}···Mn^{IV}eq	2.955(1)	2.944(18)	−0.011
Mn^{IV}···Mn^{IV}ax	2.836(30)	2.811(58)	−0.025
Mn^{IV}···Mn^{III}[c]	3.450(17)	3.460(29)	+0.0010
Mn^{IV}···Mn^{II}	3.591(14)	3.585(13)	−0.006
Mn^{IV}···Mn^{III}[d]	2.762(13)	2.779(44)	+0.018
Mn^{III}···Mn^{III}	3.367(37)	3.379(45)	+0.012
Mn^{III}···Mn^{II}	3.517(1)	3.523(2)	+0.006
Mn^{IV}–O$_c$(eq)	1.929(38)	1.923(87)	−0.006
Mn^{IV}–O$_c$(ax)	1.803(16)	1.876(44)	−0.027
Mn^{IV}–O$_r$	1.861(40)	1.872(48)	+0.0011
Mn^{III}[c]–O$_r$	1.892(18)	1.908(17)	+0.016
Mn^{II}–O$_r$	2.081(17)	2.081(7)	0.000
Mn^{III}[d]–O$_r$	1.888(24)	1.883(30)	−0.005
Mn^{III}–O$_w$	2.208(0)	2.194(20)	−0.014
Mn^{II}–O$_w$	2.217(22)	2.242(34)	+0.025
Mn^{IV}–O$_b$	1.936(11)	1.946(36)	+0.010
Mn^{III}–O$_b$(eq)	1.966(29)	1.976(45)	+0.010
Mn^{II}–O$_b$(eq)	2.148(23)	2.134(47)	−0.014
Mn^{III}–O$_b$(ax)	2.185(78)	2.179(87)	−0.006

[a] Averaged using the virtual D_{2d} symmetry of the $Mn_{12}O_{12}$ core ignoring the positioning of the water and Mn^{II} ion. [b] O$_c$ = central cubane oxygens; O$_r$ = outer ring oxygens; O$_w$ = water oxygens; O$_b$ = bridging carboxylate oxygens; ax = axial; eq = equatorial. [c] Mn atoms Mn (6, 8, 12). [d] Mn atoms Mn (5, 7, 9, 11).

Table 10. Solution ^{1}H NMR Data for [Mn$_{12}$O$_{12}$(O$_2$CR)$_{16}$(H$_2$O)$_4$]$^{0,-1}$ Complexes

R = Me, Complex **1**

δ, ppm[a] CD$_3$CN	assignment	T_1, ms
48.2(1.0)	CH$_3$(III−III) ax	3.3
41.8(1.8)	2CH$_3$ eq	3.4
18.7[b]	H$_2$O	*c*
13.9(1.0)	CH$_3$(III−V) ax	5.7

R = Et, Complex **3**

δ, ppm			
toluene-d_8	CD$_3$CN	assignment	T_1, ms
53.3	52.7(1.9)	CH$_2$(III−III) ax	2.7
50.4	47.3(4.0)[d]	CH$_2$ eq	3.1
45.1	46.7	CH$_2$ eq	2.9
12.4	12.2(4.8)[d]	CH$_2$(III−IV) ax	5.4
10.8	11.12	CH$_3$(III−III) ax	3.8
4.1	3.7(2.9)	CH$_3$(III−IV) ax	7.0
−5.2	−4.9(6.0)	2CH$_3$ eq	4.9

[PPh$_4$][Mn$_{12}$O$_{12}$(O$_2$CEt)$_{16}$(H$_2$O)$_4$], Complex **4**

δ, ppm				
CDCl$_3$	CD$_2$Cl$_2$	CD$_3$CN	assignment	T_1, ms (in CD$_3$CN)
50.2	48.9	48.0	CH$_2$(III−III) ax	2.6
45.0	44.8(2)	45.4	CH$_2$ eq	2.7
43.6		44.6	CH$_2$ eq	2.7
13.2	12.4	11.5	CH$_2$(III−IV) ax	4.2
10.4	10.2	10.2	CH$_3$(III−III) ax	2.7
3.7	3.5	3.2	CH$_3$(III−IV) ax	6.3
−3.2	−2.9	−2.7	2CH$_3$ eq	4.4

[a] Numbers in parentheses are the measured relative integration ratios. [b] The chemical shift of the water peak varies greatly due to exchange between bound and free water in solution. [c] T_1 values not measured because of exchange. [d] The integral indicated includes two peaks which are difficult to separate because of their broadness and close proximity.

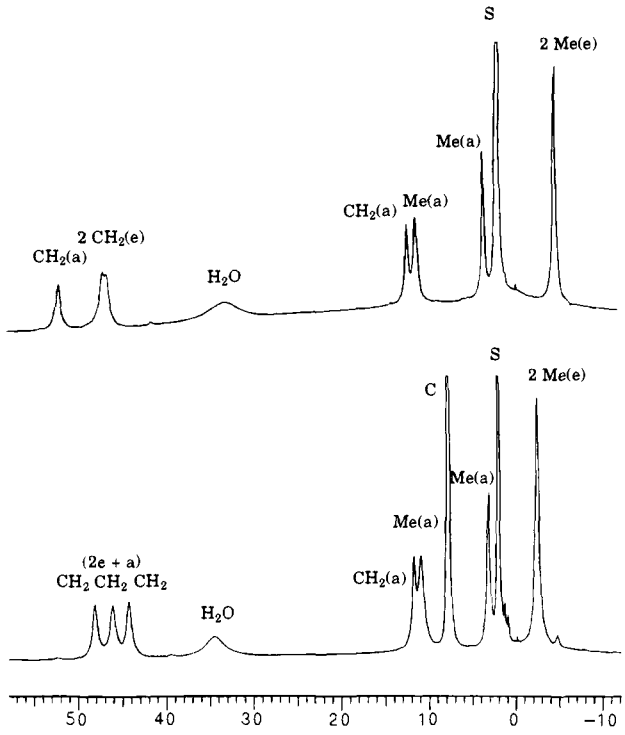

Figure 4. The ^{1}H NMR (300 MHz) spectra of CD_3CN solutions of $[Mn_{12}O_{12}(O_2CEt)_{16}(H_2O)_3]\cdot H_2O$ (**3a**) (top) and $(PPh_4)[Mn_{12}O_{12}(O_2CEt)_{16}(H_2O)_4]$ (**4**) (bottom). The solvent peak in each spectrum is marked with an S; a = axial, e = equatorial. In the case of complex **4** there is a peak marked C for the PPh_4^+ cation.

carboxylate coordinated to the Mn^{II} is apparent, and the relative integration ratios are similar to those in **3**, indicating that a peak due to the Mn^{II} is not broadened beyond observation. Thus, complex **4** exhibits the same effective symmetry in solution as **3**.

The isotropic shifts of several resonances appear to be less sensitive to reduction than the others: peaks at 3.2 and 11.5 ppm undergo very little change in isotropic shift upon reduction. As these peaks were assigned to complex **3** as arising from the CH_2 and CH_3 protons of axial carboxylates that bridge the $Mn^{III}\cdots Mn^{IV}$ pairs, this is entirely consistent with the reduction occurring at an outer Mn atom coordinated by two axial waters. If the Mn^{II} ion does indeed prefer to reside at a site in which it is ligated by two neutral axial water ligands, the shifts of the axial carboxylates should not be affected much by the additional electron, because then there would be no axial carboxylates coordinated to the Mn^{II}.

A measurement of T_1 values for complex **4** shows that the T_1 values for all peaks have decreased slightly in value. This is consistent with the presence of a Mn^{II} ion in the complex because Mn^{II} has a longer electronic relaxation time (10^{-8}–10^{-9} s for Mn^{II} *vs* 10^{-10}–10^{-11} s for Mn^{III}),[18] and thus facilitates proton relaxation and broadens the peaks. The T_1 values decrease more significantly for the carboxylates that bridge the outer ring Mn ions. This would be expected because the Mn^{II} ion is in closer proximity to the outer-ring carboxylates.

The ^{1}H NMR spectrum of a 1:1 mixture of complexes **3** and **4** in CD_3CN shows peaks due to both species, indicating that electron transfer between the reduced and neutral species is slow relative to the paramagnetic NMR time scale ($k \leq 1000\ s^{-1}$). In addition, the reduced species is stable in CD_3CN solution, showing no conversion to the neutral species over a period of 10 days. A study of the concentration dependence of the chemical shift was carried out over a range of greater than 2 orders of magnitude; however, the only peak that exhibited significant concentration dependence was the peak due to the water.

Table 11. ^{19}F NMR Data for $[Mn_{12}O_{12}(O_2CC_6H_4X\text{-}p)_{16}(H_2O)_4]$ (X = CF_3, F) in CD_3CN

X = CF_3		X = F	
δ, ppm[a]	assignment	δ, ppm	assignment
−54.8 (2.0)	eq	−83.4 (2.0)[b]	eq
−58.3 (1.0)	ax	−83.7	eq
−63.1 (0.9)	ax	−100.0 (1.1)	ax
−63.8	free acid	−107.4	free acid
		−108.8 (0.9)	ax

[a] Numbers in parentheses are the measured relative integration ratios. [b] Quoted integration ratio is the sum of the −83.4 and −83.7 ppm peaks, which are too close for separate measurement. ax = axial; eq = equatorial.

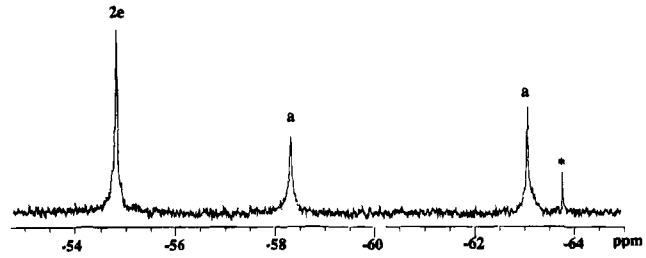

Figure 5. The ^{19}F NMR (339.7 MHz) spectrum of a CD_3CN solution of $[Mn_{12}O_{12}(O_2CC_6H_4CF_3\text{-}p)_{16}(H_2O)_4]$. The peak marked with an asterisk is a trace of free acid; a = axial, e = equatorial.

^{19}F NMR Spectroscopy. It is clear from Figure 4 that the four symmetry-inequivalent types of carboxylate groups in **3** can lead to a complicated ^{1}H NMR spectrum if each carboxylate contains more than one type of proton environment. For this reason, the even more complicated spectrum of complex **2** (12 carboxylate resonances) has not been amenable to ready peak assignment. In anticipating future reactivity studies with $[Mn_{12}O_{12}]$ complexes, which might involve a variety of added reagents and which would ideally be monitored by NMR, it is obvious that spectral simplicity would be beneficial. We have thus explored the use of ^{19}F NMR spectroscopy for these paramagnetic species, employing an appropriately chosen carboxylate such that only one resonance is obtained from each symmetry-inequivalent type. Our test-of-feasibility experiments were performed with the *p*-fluorobenzoate and *p*-(trifluoromethyl)benzoate derivatives of **2**. The results are tabulated in Table 11 and the spectrum for $[Mn_{12}O_{12}(O_2CC_6H_4CF_3\text{-}p)_{16}(H_2O)_4]$ presented in Figure 5, which shows three signals in a 2:1:1 integration ratio. On the basis of the previous analysis of the ^{1}H NMR spectra of **1** and **3**, the δ = −54.8 ppm signal is assigned to coincidental overlap of two signals from the equatorial carboxylate groups. The spectrum of the $p\text{-}FC_6H_4CO_2^-$ derivative is extremely similar, except for greater line broadening and larger paramagnetic shifts as expected from the decreased distance to the metal centers. In addition, resolution is seen in the most downfield peak, supporting its assignment as two separate but overlapping signals. Overall, it is evident that ^{19}F NMR can indeed be employed to provide spectral simplification when larger carboxylates such as benzoates are involved.

EPR Spectroscopy. In addition to being quite amenable to paramagnetic NMR studies, complex **4** is also EPR active at low temperatures. When spectra are recorded on a dilute toluene/CH_2Cl_2 glass, the complex exhibits a broad peak centered at g = 10.5. The intensity of this peak grows from 4.5 K to approximately 15 K, whereupon it begins to decrease until the peak disappears at approximately 60 K. Low-field

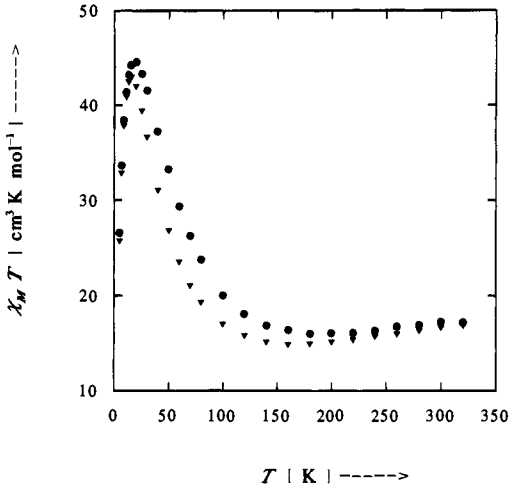

Figure 6. Plot of $\chi_M T$ versus temperature for polycrystalline samples of (●) $[Mn_{12}O_{12}(O_2CEt)_{16}(H_2O)_3]\cdot H_2O$ (**3a**) and (▼) $(PPh_4)[Mn_{12}O_{12}(O_2CEt)_{16}(H_2O)_4]$ (**4**). χ_M is the molar dc magnetic susceptibility measured at 10.0 kG.

Figure 7. Plot of reduced magnetization, $M/N\mu_B$ (N is Avogadro's number and μ_B is the Bohr magneton) vs. H/T for $[Mn_{12}O_{12}(O_2CEt)_{16}(H_2O)_3]\cdot H_2O$ (**3a**). Data were measured in the 2.0−4.0 K range and at four magnetic fields: (■) 50.0, (▼) 40.0, (●) 30.0, and (▲) 20.0 kG. The solid lines resulted from least-squares fitting of the data; see text for fitting parameters.

EPR signals, especially for a species with such a complicated magnetic structure (*vide infra*), are not well-understood. However, this feature appears to be common to glasses and solids (same signal, only broader) of all reduced $[Mn_{12}O_{12}]$ complexes.

Direct Current Magnetic Susceptibility. Susceptibility measurements carried out with a dc magnetic field have as one goal the determination of the spin for the ground state of a high nuclearity complex. Variable-temperature dc magnetic susceptibility data were collected for polycrystalline samples of complexes **3a** and **4** in an applied magnetic field of 10.0 kG. The samples were embedded in parafilm wax to prevent any torquing of the crystallites in the magnetic field. As can be seen in Figure 6, $\chi_M T$ for complex **3a** increases with decreasing temperature from 17.19 cm^3 K mol^{-1} (11.7 μ_B/molecule) at 320.0 K to a maximum of 44.57 cm^3 K mol^{-1} (18.9 μ_B/molecule) at 20.0 K, whereupon there is a decrease to 26.6 cm^3 K mol^{-1} (14.6 μ_B/molecule) at 5.01 K. All susceptibility data are available in the Supplementary Material. The data for the one-electron reduced complex **4** show a similar temperature dependence; however, the $\chi_M T$ values are less than those for complex **3a** at most temperatures. Complex **4** exhibits a maximum in $\chi_M T$ at a lower temperature of 15.0 K, where $\chi_M T$ is 43.0 cm^3 K mol^{-1} (18.5 μ_B/molecule).

If there were no magnetic exchange interactions present in a $Mn^{III}_8Mn^{IV}_4$ complex such as **3a**, then the spin-only effective magnetic moment with $g = 2.0$ should be $\mu_{eff} = 15.87\ \mu_B$. As we concluded[4] previously for complexes **1** and **2**, the increase in $\chi_M T$ with decreasing temperature to a maximum at low temperatures very likely reflects the fact that as the temperature is decreased only one spin state is thermally populated. Furthermore, this ground state must be a state with a relatively large spin. The acetate complex **1** was found[4] to have an $S = 10$ ground state, whereas the benzoate complex **2** has an $S = 9$ ground state.

In order to determine the ground-state spin for complexes **3a** and **4**, magnetization data were collected under a variety of conditions. In the first case, magnetization data were measured for polycrystalline samples of complexes **3a** and **4** in the temperature range of 2.0−4.0 K and at external fields of 20.0, 30.0, 40.0, and 50.0 kG. Figure 7 shows these data for complex **3a**, where it can be seen that at the lowest temperature and highest magnetic field there appears to be a saturation at a reduced magnetization value of $M/N\mu_B = 13.8$. If there is only one state thermally populated in the 2.0−4.0 K range in these applied fields, then the nonsuperimposition of the four isofield data sets shown in Figure 6 indicates that the ground state has appreciable zero-field splitting. In order to least-squares fit the data in Figure 7, it is assumed that a ground state of spin S is the only state populated in the 2.0−4.0 K range, and the magnetization for the complex is then calculated with eq 3:

$$M = N\sum_{i=1}^{P}(-\delta E_i/\delta H)\exp(-E_i/kT)/\sum_{i=1}^{P}\exp(-E_i/kT) \quad (3)$$

In this equation N is Avogadro's number, and $\delta E_i/\delta H$ is the change in the energy of the ith level in response to a change in a magnetic field. The energies of the various sublevels ($\pm M_S$) of the ground state are obtained by diagonalization on each iteration of the spin Hamiltonian matrix which includes the Zeeman and axial zero-field ($D\hat{S}_z^2$) interactions.

The solid lines in Figure 7 represent the least-squares fit of the four isofield magnetization data sets for complex **3a**. The best fit was found with $S = 9$, $D = 0.6$ cm^{-1}, and $g = 1.95$ for the ground state. Although the least-squares fit of the data looks reasonable, it will be shown below that there are appreciable relaxation effects present, particularly at temperatures below 3 K. Thus, it is possible that the evaluation of $S = 9$ for the ground state of complex **3a** by the above high-field magnetization data may not give a quantitatively accurate value.

The reduced magnetization *vs* H/T data obtained for complex **4** in the 20.0−50.0 kG and 2.0−4.0 K range (not shown) were least-squares fit in the same fashion to give $S = {}^{19}/_2$, $D = 0.4$ cm^{-1}, and $g = 1.74$. Again, despite the fact that the fit looks reasonable, the caveat about relaxation effects has to be raised. When the sample temperature is decreased to the lowest temperature in the presence of an external magnetic field, relaxation effects (*vide infra*) may be encountered. Following a decrease in temperature it may take a very long time (days) for the magnetization of the sample to reach an equilibrium value because of the extremely sluggish kinetics of the process. This is particularly true if there is a phase transition occurring in the temperature range under investigation. When such relaxation effects are present, then the evaluation of the spin of the ground state by using a plot $M/N\mu_B$ *vs* H/T is difficult.

Direct current magnetic susceptibility data were also collected at very low fields (5, 10, 15, 20, and 25 G) for polycrystalline

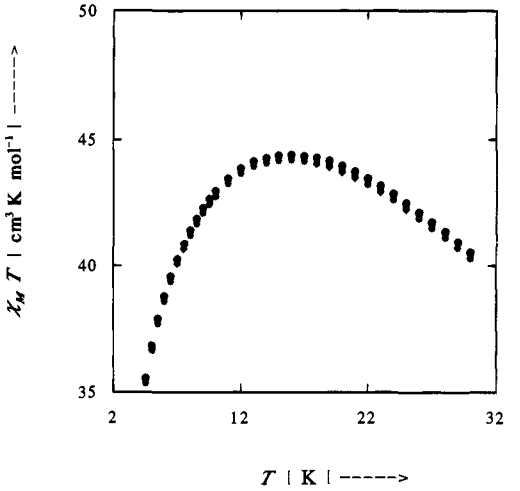

Figure 8. Plot of $\chi_M T$ *vs* temperature for a polycrystalline sample of $[Mn_{12}O_{12}(O_2CEt)_{16}(H_2O)_3]\cdot H_2O$ (**3a**) in the 4.5−30 K range. χ_M is the molar dc magnetic susceptibility measured at fields of 5.0, 10.0, 15.0, 20.0, and 25.0 G. Five different $\chi_M T$ *vs* T data sets are plotted.

samples of complexes **3a** and **4** in the 4.5−30 K range. A plot of $\chi_M T$ *vs* temperature for complex **3a** at the five different fields in the 5−25 G range is shown in Figure 8. It can be seen that all five data sets superimpose in the ~13−19 K range and there is a broad maximum with $\chi_M T \simeq 44.2$ cm^3 K mol^{-1}. If only one spin state is thermally populated and there are no appreciable intermolecular interactions, this corresponds to a complex with an $S = 9$ ground state where $g = 1.98$. DC susceptibility data for complex **4** were also collected in the 4.5−30 K range at the same five low field values. These five data sets are also superimposable with a maximum value of $\chi_M T = 46.3$ cm^3 K mol^{-1} in the 6−12 K range. This is consistent with an $S = {}^{19}/_2$ ground state with $g = 1.93$ for complex **4**.

Alternating Current Magnetic Susceptibility. In the dc susceptibility technique the static susceptibility $\chi = M/H$ is determined. In the ac susceptibility experiment the direction of the magnetic field is varied at a known frequency ν (25−997 Hz in our experiments) and the ac susceptibility is given as $\chi_{ac} = dM/dH$. The small amplitude (1−10^{-3} G) of the ac field allows an accurate determination of the magnetic microstructure, while the possibility of varying the frequency of the oscillating field adds important information about the dynamics in the magnetic system. It is possible to characterize spin−lattice relaxation, spin−spin relaxation, and cross-relaxation processes. Relaxation processes associated with phase transitions can also be probed.

The ac susceptibility of a polycrystalline sample of complex **3a** was measured in zero dc field with a 0.0050 G ac field at the frequencies of 25, 50, 100, 250, 499, and 997 Hz. In Figure 9 are shown plots of $\chi'_M T$ *vs* temperature, where χ'_M is the real part (*i.e.*, in-phase component) of the ac magnetic susceptibility. In part A of Figure 9 is a plot of the data at 50, 250, and 997 Hz in the 4.5−30 K range. There is a relatively constant value of $\chi'_M T \simeq 42.0$ cm^3 K mol^{-1} in the 11−23 K range. This corresponds to the $\chi'_M T$ value expected for a complex with an $S = 9$ ground state ($g = 1.93$). This agrees with the assessment obtained from the low-field dc data.

In part B of Figure 9 is given a plot of $\chi'_M T$ *vs* T for complex **3a** in the 2.0−10.0 K range and at all six different frequencies. Two very interesting observations can be made: first, there is systematic frequency dependence seen in these low-temperature data; second, there is a "two-step" decrease in $\chi'_M T$ when the temperature is decreased below ~7 K. As described previously,[4] the rapid decrease in $\chi'_M T$ at these low temperatures is

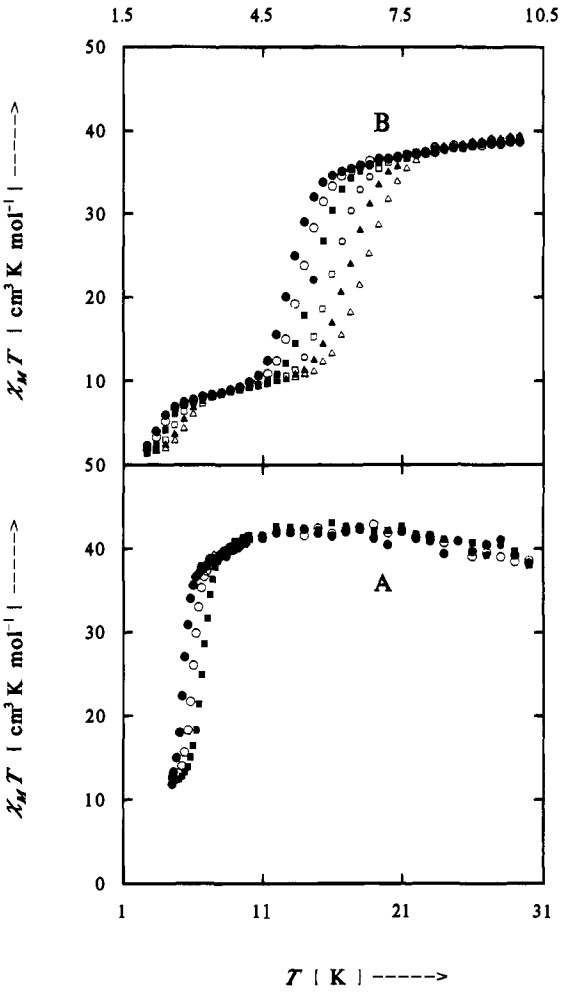

Figure 9. Plot of $\chi'_M T$ *vs* temperature for a polycrystalline sample of $[Mn_{12}O_{12}(O_2CEt)_{16}(H_2O)_3]\cdot H_2O$ (**3a**). χ'_M is the in-phase (real) component of the ac magnetic susceptibility. In part A is a plot of data obtained at (●) 50, (○) 250, and (■) 997 Hz in the 4.5−30 K range. In part B is a plot of data in the 2.0−10.0 K range measured at six frequencies: (△) 997, (▲) 499, (□) 250, (■) 100, (○) 50, and (●) 25 Hz.

attributable to a relaxation process. That is, as the temperature is decreased there is a temperature (~7 K) below which the magnetic moment (magnetization) of complex **3a** cannot stay in phase with the oscillating field. In fact, there are two different regions of relaxation in evidence, one in the 4.5−7.0 K region and one in the 2.0−3.0 K region; thus, there are two different relaxation processes.

Figure 10 clearly documents the presence of two different relaxation processes in a polycrystalline sample of complex **3a**. In this figure χ''_M is plotted *vs* temperature, where χ''_M is the out-of-phase (*i.e.*, imaginary) component of the ac magnetic susceptibility. Data are presented for six different (25−997 Hz) ac frequencies. At 499 Hz, for example, the two peaks in χ''_M *vs* T are found at 2.6 and 6.4 K. A peak in χ''_M occurs because, as the temperature is decreased, the thermal energy is reduced to a point where the magnetization of the sample cannot stay in phase with the oscillating ac field. At this point an out-of-phase component of the ac susceptibility appears. If the ac frequency is changed, there may be a change in the temperature at which the peak in χ''_M occurs. Thus, whether the ac field is oscillating slowly or rapidly could impact on how well the magnetization of the complex is able to keep in phase with the ac field. In short, ac susceptibility can be used to probe dynamics that affect the magnetic system.

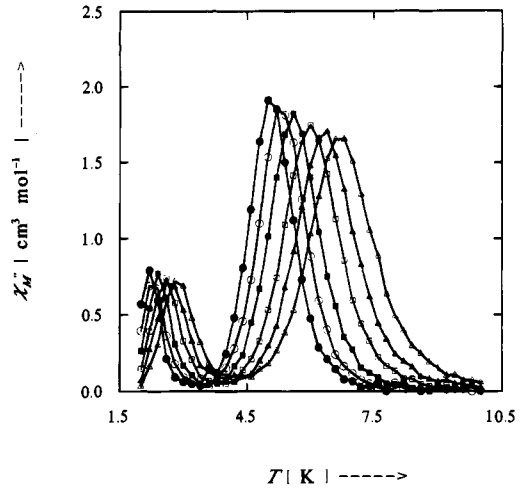

Figure 10. Plot of the out-of-phase (imaginary) component of the molar ac magnetic susceptibility (χ''_M) versus temperature for a polycrystalline sample of $[Mn_{12}O_{12}(O_2CEt)_{16}(H_2O)_3]\cdot H_2O$ (**3a**). The data were collected in zero dc field and 5.0×10^{-3} G ac field at six frequencies: (△) 997, (▲) 499, (□) 250, (■) 100, (○) 50, and (●) 25 Hz. The lines are visual guides.

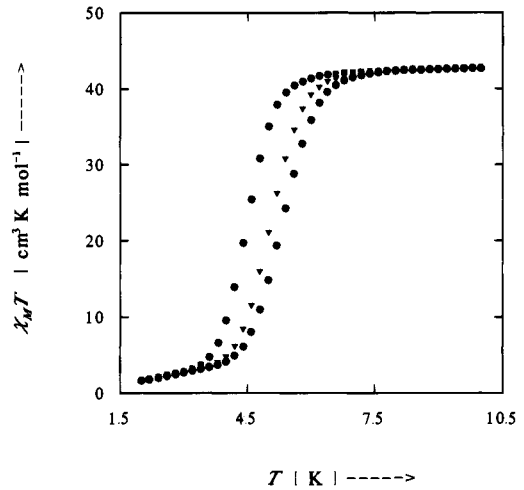

Figure 11. Plot of χ'_MT *vs* temperature for a polycrystalline sample of $(PPh_4)[Mn_{12}O_{12}(O_2CEt)_{16}(H_2O)_4]$ (**4**). χ'_M is the in-phase (real) component of the ac magnetic susceptibility. The data were collected in zero dc field and 1.0 G ac field at three frequencies: (●) 499, (▼) 250, and (■) 50 Hz.

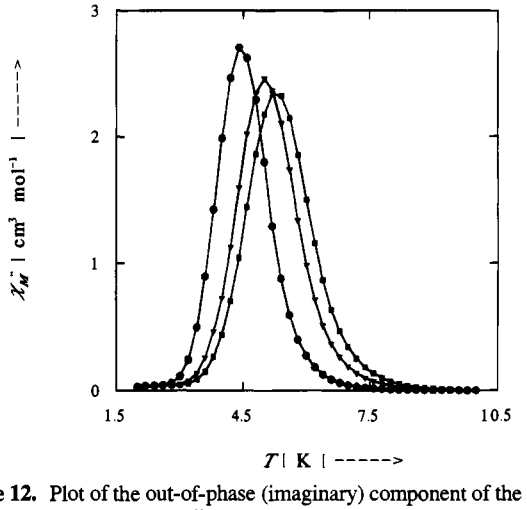

Figure 12. Plot of the out-of-phase (imaginary) component of the molar ac magnetic susceptibility χ''_M versus temperature for a polycrystalline sample of $(PPh_4)[Mn_{12}O_{12}(O_2CEt)_{16}(H_2O)_4]$ (**4**). The data were collected in zero dc field and 1.0 G ac field at three frequencies: (■) 499, (▼) 250, and (●) 50 Hz. The lines are visual guides.

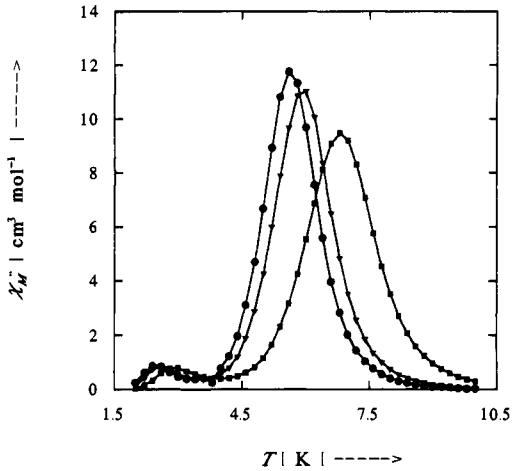

Figure 13. Plot of the out-of-phase (imaginary) component of the molar ac magnetic susceptibility (χ''_M) versus temperature for a crystal–bundle sample of $[Mn_{12}O_{12}(O_2CMe)_{16}(H_2O)_4]\cdot 2HOAc\cdot 4H_2O$ (**1**). The single crystals were bundled together and oriented in the 1.0 G ac field so that the ac field is parallel to the crystal *c* axis. This is the axis of maximum susceptibility for the crystal and for each Mn_{12} complex. The data were measured in zero dc field and at three frequencies: (■) 499, (▼) 100, and (●) 55 Hz. The lines are visual guides.

AC magnetic susceptibility data were also obtained for a polycrystalline sample of $[PPh_4][Mn_{12}O_{12}(O_2CEt)_{16}(H_2O)_4]$ (**4**) in zero dc field and either a 5.0×10^{-3} or 1.0 G ac field. The results are the same for either ac field; of course, improved signal-to-noise was obtained with the 1 G ac field. In Figure 11 is given a plot of χ'_MT *vs* temperature for complex **4** in a 1.0 G ac field. The real component of the ac susceptibility shows one abrupt decrease in χ'_MT occurring over a three-degree range. Apparently there is only one relaxation process seen for complex **4** in the 2.0–10.0 K range. This is confirmed by the plot of the out-of-phase susceptibility χ''_M versus temperature given in Figure 12. The three frequencies used in this experiment are 50, 250, and 499 Hz. As with the peaks in χ''_M seen for complex **3a**, there is a frequency dependence in the temperature at which there is a maximum in χ''_M; this temperature decreases as the frequency is decreased. At the three frequencies used for complex **4**, the temperatures for a maximum in χ''_M are 5.2 K (499 Hz), 5.0 K (250 Hz), and 4.4 K (50 Hz). The magnitude of the shift in χ''_M maximum temperature is comparable to that seen for complex **3a** (see Figure 10).

Previously the acetate complex **1** and the benzoate complex **2** were reported[4,5] to show only one peak in their plots of χ''_M *vs* temperature, and we therefore recollected data for both complexes. For the acetate complex **1**, ac data were obtained on a polycrystalline sample in both 1.0 and 5.0×10^{-3} G ac fields. Since the acetate complex can be grown in a relative large crystal form, we also ran data for a sample consisting of a bundle of 10 large crystals held together in the same orientation. The experiments on the polycrystalline and crystal–bundle samples gave the same results. In Figure 13 are shown the ac susceptibility data for the crystal–bundle sample of complex **1** in a 1.0 G ac field. The crystals are oriented so that the ac field is parallel to the crystal *c* axis ($I\bar{4}$ space group). The *c* axis is the easy axis of the crystal, *i.e.*, the direction of the largest component of the crystal's magnetic susceptibility tensor. All molecules are oriented parallel in the crystal and, thus, the ac field is oriented parallel to the "axial" direction for

each molecule. As can be seen in Figure 13, there are clearly two relaxation processes present in the acetate complex, and in the plot of χ''_M *vs* T there are two peaks, one of which is considerably less intense than the other. At 499 Hz, the two peaks occur at 6.8 and 3.0 K, whereas at 55 Hz they are at 5.6 and 2.4 K. In the previous ac experiments[4,5] a polycrystalline sample of complex **1** was examined in the 4−25 K range; it is thus understandable why the lower temperature peak was not seen. Those experiments were carried out on a home-built ac susceptometer operating in the earth's field and one peak was seen at 7.0 K for 500 Hz ac field and at 5.4 K for 55 Hz.

Alternating current experiments were also carried out on a polycrystalline sample of the benzoate complex **2**. With a 1.0 G ac field, a strong out-of-phase peak is seen at 5.8 K with a 499 Hz frequency. It shifts to 5.2 K when the frequency is changed to 100 Hz. Upon close examination there does appear to be a second extremely weak peak at ~2.4 K for 500 Hz and at ~2.1 K for 100 Hz. In summary, complexes **1**, **2**, and **3a** each show two out-of-phase ac signals where the lower temperature one is of low intensity for complexes **1** and **2**. The reduced complex **4** only shows one peak, but a second lower-temperature peak, if there is one, may occur below 2 K.

Polymer-Doped Complex 3a. Since the propionate complex **3a** is the most soluble of the complexes used in this study, it was selected as a candidate for preparing a polymer-doped sample to see if doping complex **3a** might affect the out-of-phase ac signal. Such an experiment can be used to ascertain whether the out-of-phase ac signals are due to a relaxation process involving individual complexes, or a process involving large collections (domains) of complexes. Complex **3a** and polystyrene (average MW = 280 000) were dissolved in CH_2Cl_2, and evaporation of the solution gave a film. Two different polystyrene-doped samples were prepared, one where complex **3a** was present at 54 wt % and the other with complex **3a** at 3.6 wt %. In the latter case the polystyrene film looked quite transparent, whereas in the case of the higher concentration film there were some darker regions.

Two out-of-phase ac susceptibility signals were seen for both of the polystyrene-doped samples. The ac data obtained for the 3.6 wt % doped sample are shown in Figure 14. A frequency dependence is seen, as with the nondoped samples. Doping of complex **3a** into polystyrene results in a shift in temperature of the peak maxima. There is also a change in the relative intensities of the two peaks, the origin of which is not known. With the ac frequency set at 499 Hz, the polycrystalline sample shows peaks at 6.4 and 2.6 K. These peaks shift to 5.8 and 2.4 K for the 54 wt % sample and then to the lowest temperatures of 4.2 and 2.0 K for the 3.6 wt % sample. Since the 3.6 wt % polystyrene-doped sample was optically transparent, it is reasonable to conclude that the Mn_{12} molecules are well-separated, assuming that the polymer doping is homogeneous. This is one piece of evidence to indicate that the origin of the two relaxation processes is within individual molecules.

Hysteresis Effects. Polycrystalline samples of complexes **3a** and **4** were examined for hysteresis effects by employing the dc susceptometer. In the first experiment, the susceptometer was de-Gaussed and then a sample introduced and cooled to 2 K. After thermal equilibration, a magnetic field of 100.0 G was applied and the magnetization of the sample was measured as the temperature was increased from 2.0 to 6.0 K, and then decreased from 6.0 to 2.0 K. The results for complexes **3a** and **4** are shown in Figure 15. For both complexes there is a difference in the zero-field-cooled (ZFC) and the field-cooled (FC) magnetization. The slow relaxation of the magnetization

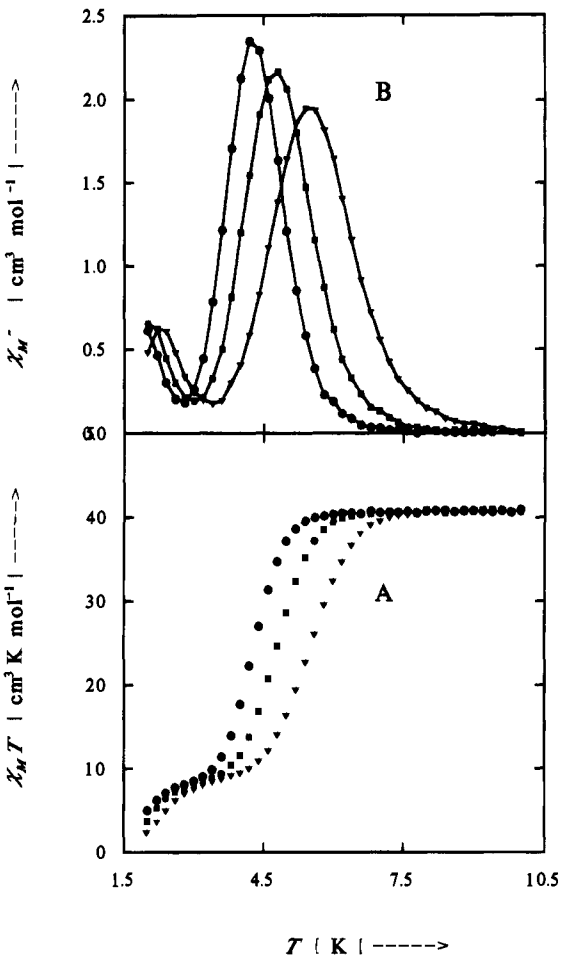

Figure 14. Plot of ac magnetic susceptibility data versus temperature for polystyrene-doped (3.6 wt %) sample of $[Mn_{12}O_{12}(O_2CEt)_{16}(H_2O)_3]\cdot H_2O$ (**3a**). In part A, $\chi'_M T$ is plotted *vs* the temperature, where χ'_M is the in-phase (real) component of the ac susceptibility. In part B the out-of-phase component χ''_M of the ac susceptibility is plotted versus T. The data were collected in zero dc field and an ac field of 0.50 G at three frequencies: (▼) 499, (■) 100, and (●) 50 Hz. The lines are visual guides.

is responsible for the large difference between the ZFC and FC magnetization data.

For complex **3a** (Figure 15A) the ZFC and FC magnetization curves become superimposed at 3.0 K. This happens to be the same temperature reported[5] for ZFC and FC data of a single crystal of complex **1**. In the ZFC cycle when the temperature is decreased below 3.0 K, the magnetization is "frozen" on the time scale of the experiment. If, for example, the temperature was cooled to 2.5 K in the ZFC cycle, then over a long period of time the magnetization would increase in value to eventually reach the value found on the FC curve at 2.5 K. The system would relax to an equilibrium value. In the previous work on complex **1**, Sessoli *et al.*[5] concluded that since the 3.0 K temperature does *not* correspond to an anomaly in the relaxation times, it is not associated with a magnetic phase transition. However, with our new ac susceptibility experiments on the acetate complex **1** (Figure 13), it is now apparent that there is indeed a relaxation process centered at 2.8 K.

For complex **4** (Figure 15B) the ZFC and FC magnetization curves become superimposed at 4.6 K. The ZFC magnetization curve looks different than that for complex **3a**; there is an inflection point at ~2.5 K and above that a more gradual approach of the ZFC curve to the FC curve. The 4.6 K temperature is the same as the 4.6 K temperature observed for

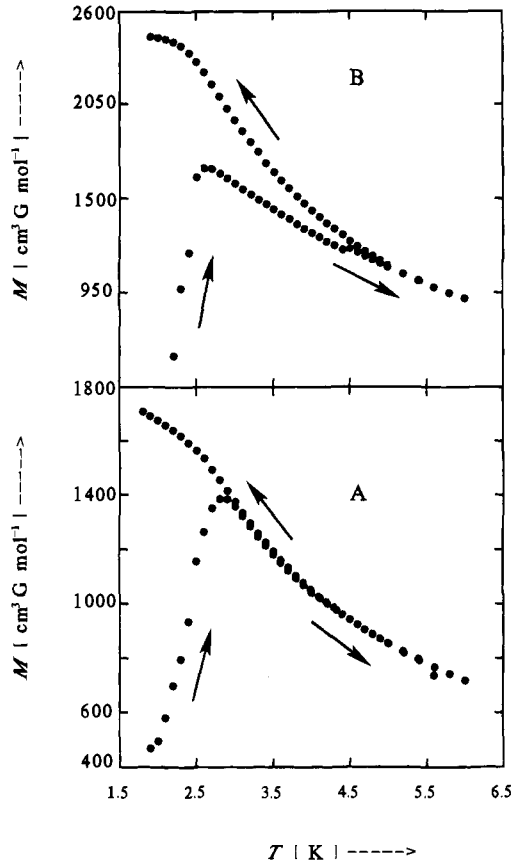

Figure 15. Temperature dependence of the dc magnetization of polycrystalline samples of (A) $[Mn_{12}O_{12}(O_2CEt)_{16}(H_2O)_3]\cdot H_2O$ (**3a**) and (B) $(PPh_4)[Mn_{12}O_{12}(O_2CEt)_{16}(H_2O)_4]$ (**4**). Each sample is first cooled to 2.0 K in zero field, then a 100.0 G field is applied and the magnetization is measured as the temperature is increased to 6.0 K to give the zero-field-cooled (ZFC) data. This is then followed by cooling the sample from 6.0 to 2.0 K with the 100.0 G field maintained to give the field-cooled (FC) data.

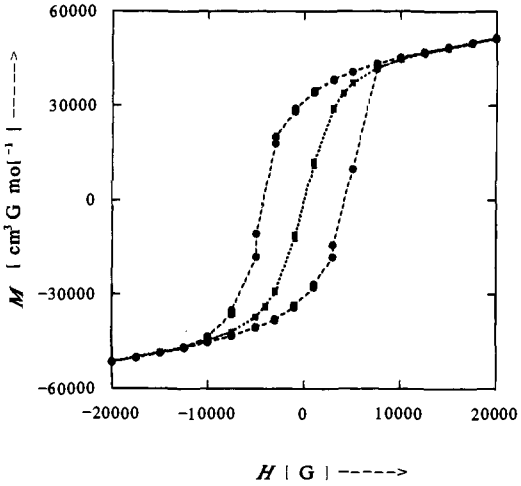

Figure 16. Hysteresis loops for a polycrystalline sample of (PPh_4)-$[Mn_{12}O_{12}(O_2CEt)_{16}(H_2O)_4]$ (**4**) measured at (●) 2.2 and (■) 2.8 K. The 2.8 K loop was measured first.

the out-of-phase ac signal observed for complex **4** at the lowest measurement frequency of 50 Hz (see Figure 12).

Complex **4** also exhibits a hysteresis loop, as shown in Figure 16. At 50.2 mg polycrystalline sample was dispersed in vaseline and then cooled to 2.8 K in zero field. After thermal equilibration, the magnetic field was increased to 20.0 kG. The magnetization was measured as the magnetic field was decreased to zero and then reversed in direction and increased to −20.0 kG. This was followed by cycling the field back from −20.0 kG to zero, then to 20.0 kG. As can be seen in Figure 16, there is no hysteresis seen for complex **4** at 2.8 K. After the 2.8 K loop was finished, the sample was cooled to 2.2 K in the 20.0 kG field and a complete loop (20.0 kG ↔ −20.0 kG) determined at 2.2 K. At this lower temperature there is a well-developed hysteresis loop seen. At 2.2 K, the coercivity is 4062 G. When H is reduced from saturation at 20.0 kG to zero field, the magnetic induction goes from a saturation value B_s to a remanent magnetization B_r of 3.30×10^4 cm³ G mol⁻¹.

The existence of a hysteresis loop in the response of magnetization to an external magnetic field is, of course, a reflection of the presence of some kinetic process. For ferromagnets or ferroelectrics, for example, the presence of domain structure is required to give hysteresis. As the field is increased, the domains with moments misaligned are consumed by the domains with their moments favorably aligned. It is the kinetics associated with the domain wall movement (boundaries between regions) that dictate whether a hysteresis loop is seen and the shape of the loop. For ferromagnets and ferroelectrics, there are interactions between centers, and long-range order develops. Is it possible that each molecule in a polycrystalline sample of complex **4** exhibits a hysteresis loop? That is, the intermolecular interactions in complex **4** are *not* appreciable. Can each molecule have such a large magnetic anisotropy due to appreciable zero-field splitting in the high-spin ground state of complex **4** that it shows a hysteresis loop as a single molecule response?

A polycrystalline sample of complex **3a** also exhibits a hysteresis loop (Figure 17A). A 19.2 mg sample was dispersed in vaseline and cooled to 2.8 K in zero field. Then, a 20.0 kG magnetic field was turned on and the magnetization monitored as the field was cycled to −20.0 kG and then back to 20.0 kG. In contrast to complex **4**, complex **3a** exhibits a small hysteresis loop at 2.8 K with a coercivity of $H_c \simeq 310$ G. A single crystal of complex **1** was reported[5] to exhibit a larger hysteresis loop at 2.8 K than for **3a**. The coercivity of the single crystal of **1** at 2.8 K was reported to be $H_c \simeq 2140$ G. The relaxation process leading to the hysteresis loop at 2.8 K for complex **3a** is probably also responsible for the low-temperature peak (2.2 K at 50 Hz; 2.8 K at 1000 Hz) seen in the plot of out-of-phase ac susceptibility χ''_M versus temperature.

The hysteresis responses of the two polystyrene-doped samples of complex **3a** were also determined. In Figure 17B magnetization versus magnetic field plots are given for the 3.6 wt % sample at 2.2 and 2.8 K. Very similar data were obtained for the 54 wt % sample. Not only does complex **3a** exhibit hysteresis loops at 2.2 and 2.8 K, but the shape and H_c values are not affected by diluting complex **3a** in polystyrene. It would appear that, if complex **3a** is homogeneously dispersed in the polystyrene, then the hysteresis loops seen for the 3.6 wt % sample indicate that this hysteresis phenomenon is attributable to isolated molecules.

Concluding Comments

Electrochemical data have been presented to show that several different $Mn^{III}_8Mn^{IV}_4$ complexes with the composition $[Mn_{12}O_{12}(O_2CR)_{16}(H_2O)_4]$ can be reversibly reduced and oxidized. A detailed characterization of $[Mn_{12}O_{12}(O_2CEt)_{16}(H_2O)_3]$ (**3**) and $(PPh_4)[Mn_{12}O_{12}(O_2CEt)_{16}(H_2O)_4]$ (**4**), including X-ray structures, has been given. Several interesting observations have been made. The structure of complex **4** shows that the added electron is localized on an outer (originally Mn^{III}) ion rather than an inner (cubane) Mn^{IV} ion, producing a trapped-valence

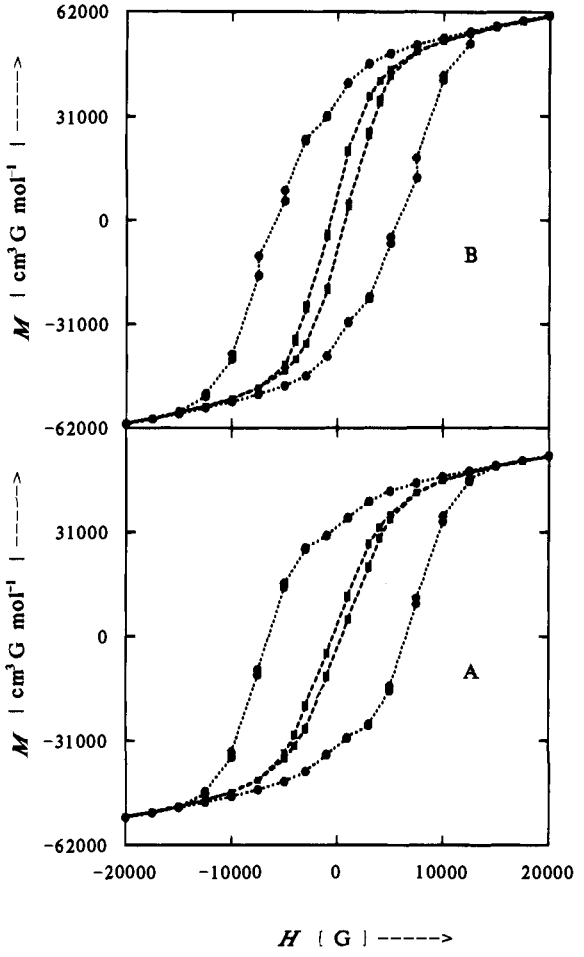

Figure 17. Hysteresis loops for $[Mn_{12}O_{12}(O_2CEt)_{16}(H_2O)_3]\cdot H_2O$ (**3a**) at (●) 2.2 and (■) 2.8 K. In part A are the data for a polycrystalline sample dispersed in vaseline. In part B are the data for a 3.6 wt % polystyrene-doped sample of **3a**.

$Mn^{II}Mn^{III}_7Mn^{IV}_4$ anion. ^1H NMR data show that there is an intramolecular dynamic process involving valence detrapping (site of Mn^{II} ion moving around eight equatorial Mn sites) and carboxylate/H_2O ligand exchange. Perhaps the most interesting observation is that complexes **3** and **4** exhibit magnetic susceptibility relaxation phenomena at low temperatures. Complex **3** and the analogous acetate (**1**) and benzoate (**2**) complexes exhibit two out-of-phase ac magnetic susceptibility peaks. Complex **4** only shows one out-of-phase ac signal. Both complexes **3** and **4** exhibit hysteresis at low temperatures. Since the hysteresis and other relaxation phenomena of complex **3** are not affected by diluting the complex in polystyrene, the hysteresis phenomenon appears to be due to isolated molecules. This same conclusion was made for the acetate complex **1** by Caneschi *et al.*[6] They based their conclusion on the absence of signs of magnetic ordering in their magnetization, susceptibility and heat capacity data for complex **1**. In particular, they found no thermal anomaly in heat capacity data for complex **1** measured down to 1.6 K.

The observation of hysteresis for individual molecules is quite unusual, and this molecular bistability may provide the means to store information at the molecular level. The molecular bistability that these $Mn^{III}_8Mn^{IV}_4$ and $Mn^{II}Mn^{III}_7Mn^{IV}_4$ complexes exhibit is due to a large molecular magnetic anisotropy. Each complex has a large-spin ground state ($S = 9$ for complex **3a** and $S = 19/2$ for complex **4**), and there is appreciable zero-field splitting in these ground states. This zero-field splitting arises from the single-ion zero-field splitting of the Mn^{III} ions that are present in each complex; the Jahn–Teller axes (sense of zero-field splitting) of the Mn^{III} ions in each complex are aligned and this gives a resultant large zero-field splitting in the ground state. The interaction (Zeeman and zero-field) is very different when the magnetic field is oriented parallel to the magnetic z axis of a complex than when it is oriented perpendicular to the z axis. When there is little thermal energy at low temperatures, there is an appreciable relaxation time for the relaxation of the magnetization of an individual molecule as the magnetic field is moved from one direction to another.

Attempts to isolate an oxidized $[Mn_{12}O_{12}]$ complex, *viz.* a salt of $[Mn_{12}O_{12}(O_2CR)_{16}(H_2O)_4]^+$ are currently in progress; it will be extremely interesting to assess the properties of a third oxidation level of these most unusual complexes.

Acknowledgment. This work was supported by NSF grants CHE-9115286 (D.N.H.) and CHE-8808019 and CHE-9311904 (G.C.). The ac magnetic susceptibility measurements were performed with an AC SQUID susceptometer provided by the Center for Interface and Material Science, funded by the W. A. Keck Foundation. We thank J. C. Huffman for the room temperature crystallographic data on complex **4**. H.J.E. was supported by an NSF Predoctoral Fellowship.

Supplementary Material Available: Tables of magnetic susceptibility and magnetization data, complete listings of bond lengths and angles, and positional parameters for complexes $3\cdot 4H_2O$ and **4** (88 pages); tables of observed and calculated structure factors (76 pages). This material is contained in libraries on microfiche, immediately follows this article in the microfilm version of the journal, and can be ordered from the ACS; see any current masthead page for ordering information.

JA942616S